NATIONAL ADVISORY COMMITTEE FOR AERONAUTICS

TECHNICAL MEMORANDUM

No. 1115

PRESSURE DISTRIBUTION MEASUREMENTS AT HIGH SPEED AND OBLIQUE INCIDENCE OF FLOW

By A. Lippisch and W. Beuschausen

Translation

Druckverteilungsmessungen bei Hochgeschwindigkeit und Schraganblasung

Forschungsbericht Nr. 1669

Washington

March 1947

NATIONAL ADVISORY COMMITTEE FOR AERONAUTICS

TECHNICAL MEMORANDUM NO. 1115

PRESSURE DISTRIBUTION MEASUREMENTS AT HIGH SPEED AND OBLIQUE INCIDENCE OF FLOW*

By A. Lippisch and W. Beuschausen

CONTENTS IN BRIEF

The present report contains the results of a series of observations obtained for a wing of symmetrical profile for different angles of yaw. The shock tunnel with 0.4m × 0.4m cross section, of the Institute for Gas Dynamics at L.F.A. - Braunschweig was available for this work.

The profile used was a 9 percent, thick hyperbolic profile with maximum thickness 40 percent aft, which was calculated by the method of F. Ringleb (2). Since the conformal transformation of this profile is known, the theoretical pressure distribution could be determined exactly for the case of incompressible flow. Then by the use of the Prandtl rule one may extend the comparison of theory and experiment to the case of higher velocity of incident flow.

TABLE OF CONTENTS

*"Druckverteilungsmessungen bei Hochgeschwindigkeit und Schräganblasung," Zentrale für wissenschaftliches Berichtswesen der Luftfahrtforschung des Generalluftzeugmeisters (ZWB) Berlin-Adlershof, Forschungsbericht Nr. 1669, VerfaBt bei Messerschmitt A.-G., Augsburg Abtlg. "L," Augsburg, den 25.9.42.

I. REASONS FOR THE INVESTIGATION

It was known, from theoretical considerations respecting a wing with oblique flow incidence, that the oblique flow incidence caused by sweepback would have very favorable effect on drag, in the region of higher speeds (1). These theoretical conclusions have recently been confirmed by high-speed measurements of swept-back wings. Hence, it seemed desirable to carry out pressure-distribution measurements in a high-speed tunnel in order to get more light on the effect of oblique incidence of flow.

II. THE MODEL AND THE EXPERIMENTAL ARRANGEMENTS

The wing model had a chord of 80 millimeters and was made in a similar way to the model with flaps tested by us in the same tunnel (3). At the midsection, along the top and bottom surfaces, there were a number of pressure holes. Figure 1 shows the profile section as well as the three orientations of the wing in the wind tunnel. For oblique flow incidence, then, the section where the measurements were taken was oblique to the direction of flow and perpendicular to the span axis. As described in reference 3, the wing was held

laterally in rotable jaws installed in the side of the tunnel. This arrangement was also used for the experiments in yaw, so that the angle of attack is defined as the angle perpendicular to the span axis. The measurements were carried out in the same way described in detail in our first report. No tunnel-wall corrections were made; that is, correction for the finite extent of the jet of air.

III. DISCUSSION OF THE EXPERIMENTAL RESULTS

(a) Angle of Yaw $\beta = 0$.- Figures 2 to 5 give the measured pressure distributions for zero angle of yaw. In order to minimize experimental error the pressure distribution was measured at both positive and negative angles of attack. Comparing the two series of observations, it was found that there were small errors in the setting of the positive angles of attack, and that construction errors were present on the top side of the wing. For these reasons, the runs at negative angle of attack are presented in this section and in all the following sections; thus, the upper surface of the wing is used as the pressure side and in this way the accuracy of measurement is not very much impaired.

The pressure-distribution measurements at zero yaw show essentially the same phenomena that are known from numerous earlier measurements of other investigators. Here it is noteworthy that the hyperbolic profile, which is especially well shaped to minimize local excess velocity, permits a shock-free flow to comparatively high Mach number.

From the measured pressure distributions, c_n and c_m are determined in the usual manner. Figure 6 gives the graph of normal-force coefficient versus Mach number at constant angles of attack. As is already known from other measurements, the increase of lift with compressibility acting is in agreement with the Prandtl rule. A family of curves drawn in the figure shows this. This agreement lasts until the velocity of sound is reached locally at the place on the profile contour of maximum velocity. This limit is indicated by the dotted curve. From there on the lift begins to increase more steeply than predicted by the Prandtl rule, but the lift subsequently goes into a steep decrease. This phenomenon

is also known from numerous earlier measurements. The same thing may be noted in the variation of the moment coefficient with Mach number. (See fig. 7.)

Figures 8 and 9 give the variation of c_n with angle of attack and also the graph of c_m versus c_n which determines the position of the center of pressure. If one fairs the curves with straight lines and determines the slope at the origin, one obtains the curves given in figure 10. The lift curve slope $dc_n/d\alpha$ in its dependence on Mach number should, according to the theory, likewise obey the Prandtl rule. One sees from the graph that at high Mach numbers this is no longer the case but that there is present an essentially greater increase of lift. This deviation from the Prandtl rule may, however, be explained if one considers that for measurements in the closed tunnel, the decrease of cross section caused by the model produces an increase of velocity at the location of the wing relative to the velocity corresponding to M_o, which is descriptive of the undisturbed flow ahead of the wing. A correction to the Mach number (fig. 11) may be derived (4) from the dimensions of the tunnel and of the model which takes care of this constriction effect. Then the corrective curve given in figure 10 shows a very good agreement with the Prandtl rule.

The position of the neutral point is indicated by the graph of dc_m/dc_n versus the Mach number. One sees that a change in position of the center of pressure does not take place until the super critical region is reached, that is, until a compression shock occurs. Compared to other measurements this feature of the experimental results is worthy of note and may well be due principally to the favorable shape of the wing profile.

(b) Angle of Yaw $\beta = 20^\circ$.- Figures 12 to 15 give the experimental pressure distributions for the wing at an oblique setting of 20°. In the plots there will be found on the axis of ordinates specially marked the values of p/q corresponding, on the one hand, to the greatest possible excess of pressure ($M = 0$) and, on the other hand, to the local incidence of the velocity of sound ($M = 1.0$). As a result of the oblique incidence of flow, these limiting values require a correction compared with the corresponding values of wing at zero yaw, since the effective Mach number for the wing in yaw is

decreased by the cosine of the yaw angle. In this way the pressure coefficient at a stagnation point is calculated to be:

$$\left(\frac{\Delta p}{q_o}\right)_{M=0} = \frac{2}{K \times M_o^2}\left[\left(1 + \frac{K-1}{2} M_o^2 \times \cos^2\beta\right)^{\frac{K}{K-1}} - 1\right]$$

Actually, for the wing in yaw a stagnation point is no longer formed, since the flow at the leading edge goes to one side as well as to the rear. Figure 45 shows the maximum pressure coefficient $\Delta p/q_o$ for $M = 0$ at the three angles of yaw at which measurements were taken.

Taking into account the oblique incidence of flow, the value of the pressure coefficient $\Delta p/q_o$, corresponding to the local occurrence of the velocity of sound ($M = 1$) is:

$$\left(\frac{\Delta p}{q_o}\right)_{M=1.0} = \frac{2}{K \times M_o^2}\left[\left(\frac{2}{K+1} + \frac{K-1}{K+1} \times M_o^2 \cos^2\beta\right)^{\frac{K}{K-1}} - 1\right]$$

Figure 46 is a graph of this function for the three values of yaw angle used. From this figure one sees the considerable extension of the subcritical region, especially at large Mach number, since on account of the yaw the critical pressure coefficient permits considerably higher Mach numbers to be reached before the velocity of sound occurs locally. Thus the pressure-distribution measurements at 20° yaw show a significant improvement of properties at high Mach numbers. The decrease of excess velocities, which indeed is to be expected even for incompressible flow as a result of the yaw (5), is evident in the case of high velocity, that is, with the influence of compressibility present, to a greater degree than would be expected from potential flow theory.

It may be remarked that some of the pressure holes in the nose got stopped up at angles of attack 1°, 2°, and 3°. Hence, the curves are represented with a dash line in this region.

Various quantities calculated from the measurements are contained in figures 16 to 20. The variation of c_n with the Mach number for constant angles of attack has become essentially less rapid than for the case of zero yaw. (See fig. 16.) If in the Prandtl rule, one takes into account the oblique flow, one gets the lift increase represented by the family of curves drawn on the figure. The agreement may be regarded as satisfactory although it is noteworthy that individual curves show a less rapid increase than is predicted by the theory. The dashed boundary curve shown indicates again those Mach numbers at which the velocity of sound occurs for the first time. For the variation of c_m with the Mach number (fig. 17) the agreement with the theoretical curves is better. If one were to obtain the values of c_m between the Mach numbers of 0.7 and 0.8 by extrapolating the measurements obtained at small Mach numbers, one would, in general, obtain slightly smaller values than those actually measured. This phenomenon which may also be observed for $\beta = 40^\circ$ indicates an influence of oblique flow incidence which has not yet been explained. The lift curve slope increases more rapidly with the Mach number than would be predicted by the Prandtl rule. But this may also be explained by the constricted flow at the location of the wing. To be sure, in the case of oblique flow incidence, the constriction effect would not be present to such a great extent, so that the correction valid for zero yaw is no longer valid. The curve dc_m/dc_n shows initially a slight forward displacement of the center of pressure. This phenomenon is likewise patently connected with the oblique incidence.

(c) Angle of Yaw $\beta = 40^\circ$.- The experimental pressure distribution for $\beta = 40^\circ$ are given in figures 21 to 24. The reduction of pressure as a result of yaw is for $\beta = 40^\circ$ already so large that at small angles of attack compression shocks are completely avoided, although measurement could be continued to considerably higher Mach numbers than is the case of the wing at zero yaw. Not until M_o is approximately 0.94 or 0.96 are separation phenomena which are caused by a compression shock to be observed. The change of pressure distribution, which is obviously caused by a shock, leads one to conclude, however, that in the case of oblique flow incidence there are other influences acting than in the case of zero yaw. For to a first approximation one would expect the pressure distributions

for zero yaw and for yaw different from zero to agree if the effective Mach numbers were taken into account. Below the critical Mach number this is actually the case. It is, however, to be noted that this agreement no longer exists after the velocity of sound has been reached locally on the suction side of the profile, at least for the larger sweepbacks.

Various quantities calculated from the pressure distributions attained at $\beta = 40^\circ$ are collected in figures 25 to 29.

Variation of normal force with Mach number at constant angles of attack showed a weaker increase than would be predicted from the Prandtl rule, taking into account the oblique flow incidence. The increase of lift at high Mach numbers, which in a case of zero yaw first takes place when the velocity of sound is reached locally, is apparent in the case of oblique flow incidence before this critical limit is reached, even though it is not strongly developed. The subsequent decrease of the lift either coincides with the boundary curve or takes place before the boundary curve is reached. On the whole, however, the influence of high speed on the normal force at $\beta = 40^\circ$ is markedly diminished, which permits the unequivocal conclusion that one will obtain essentially more favorable relations at high speed by means of sweepback. At $\beta = 40^\circ$ the effect on the moment coefficient is likewise still very small. Here again there is a small deviation of the observations from the Prandtl rule. Also the lift curve slope $dc_n/d\alpha$ up to the vicinity of $M_o = 0.7$ is flatter than would be predicted by the Prandtl rule. In the region of high Mach numbers the position of the neutral point shows a pronounced forward displacement which we have observed to a less marked extent for the 20° yaw. Thus the results of the measurements not only confirm the theory but are slightly more favorable than the theory when it comes to ameliorating the effect of high speed.

IV. COMPARISON OF SOME QUANTITIES CALCULATED FROM THE MEASUREMENTS

Figures 30 to 33 give a comparison of certain quantities calculated from the experimental pressure

distributions for the three angles of yaw. It is especially noted that the neutral point is displaced to the rear under the influence of yaw. The cause of this displacement of the neutral point is not yet explained. Figures 32 and 33 show the normal-force coefficients - and the moment coefficients - plotted versus the effective Mach number for the different angles of yaw. If the approximation used were unconditionally valid, the curves for the three angles would coincide, or there could only be a small parallel displacement of the curves as a result of error in setting the angle of attack. From this point of view, the agreement of the measurements with each other is satisfactory up to the neighborhood of $M_o \cos \beta = 0.65$. From this point on, the special influences of yaw, which we have already alluded to, become so strong that the curves deviate from each other to an essential extent. This is especially true for the measurements at $\beta = 40°$. To what extent this different behavior of the wing in yaw is connected with the circumstance that the measurements were carried out in a closed tunnel cannot be determined. It is, however, probable that a portion of the deviations may be attributed to this.

V. COMPARISON OF CERTAIN PRESSURE DISTRIBUTIONS

In figures 34, 35, and 36 certain experimental pressure distributions are plotted on the same sheet, including the correction for yaw, for purposes of comparison. According to theory the curves on one graph should coincide. Although the agreement at $\beta = 20°$ is very satisfactory, the measurements at $\beta = 40°$ show a systematic displacement in the direction of larger pressure deficiencies. The form of the pressure variation and also the total lift which is represented by the area of the curve are practically unchanged. This observed change of the pressure distribution for $\beta = 40°$ obviously must be caused by an increase of the velocity on the upper and lower side of the profile. One would probably not be wrong in assuming that the augmented velocity in the case of oblique flow incidence is caused by a thickening of the boundary layer. This thickening of the boundary layer is itself caused by the lateral flow of boundary-layer material from wing sections lying farther forward in the direction of the flow. In figure 36 two pressure distributions are compared which were made above the critical region. Unfortunately the

result to be expected for $\beta = 40^\circ$ could not be reached since in this case the pressure distribution would have had to be measured above $M_o = 1$. The agreement for $\beta = 0^\circ$ and $\beta = 20^\circ$ is comparatively satisfactory. In the region of the highest velocities the measurement at $\beta = 20^\circ$ shows greater pressure deficiencies. This may also be explained by the presence of a thicker boundary layer.

VI. COMPARISON OF THEORETICAL AND MEASURED PRESSURE DISTRIBUTIONS

Figures 37 to 44 give a comparison of the theoretical pressure distribution and the results of measurement for the wing at zero yaw and different Mach numbers. The calculated pressure distributions for incompressible flow were modified by the Prandtl factor corresponding to the Mach number in question. Although in general there is a satisfactory agreement in the whole extent of the loops especially at small Mach numbers, there are especially at the nose of the wing essential deviations between theory and measurement which without doubt are to be attributed to an inaccuracy in the fabrication of the small wing model. In particular, it is seen that the calculated pressures near the leading edge are larger than the measured values at these places. A complete agreement between the model and the theoretical profile form is extraordinarily difficult to achieve in the vicinity of the nose for at these places the smallest differences in the profile form must produce essential change in the velocity distribution. Taking into consideration these circumstances, the agreement may be regarded as satisfactory.

VII. SUMMARY

In this report are given the results of measurements made on a symmetrical wing profile of 9 percent thickness, at 0°, 20°, and 40° yaw which were obtained in the high-speed tunnel of the Institute for Gas Dynamics at LFA - Braunschweig. Taking into account the known theoretical influence of yaw, a comparison of the measurements with each other is undertaken which discloses certain systematic

deviations between theory and measurement. On the other hand the pressure-distribution measurements make possible a comprehensive insight into the flow phenomena which are produced by oblique flow incidence. The results confirm unequivocally the beneficial effect of yaw in the high velocity region.

Translated by H. R. Grummann
McDonnell Aircraft Corporation

BIBLIOGRAPHY

1. A. Buseman: Aerodynamic Lift at Supersonic Speed Convegno di Scienze Fisiche, Mathematiche e Naturali 30. Sept. - 6. Okt 1935 XIII Roma. Reale Accademie d'Italia 1936 XIV (Voltatagung) = Yoltd Congress.

2. F. Ringleb: A New Class of Profiles with Known Flow (Prepared in Manuscript 1939 - Messerschmidt Joint Stock Co. - Augsburg)

3. W. Beuschausen and J. Hubert: Pressure Distribution Measurements at High Velocities on Profile NACA-0009-62 With Cambered Flap of 25 percent Chord (Prepared in Manuscript 1940 - Messerschmidt - Augsburg)

3. J. Hubert: (Same Title) Meeting Report of the Lilienthal Society 127/43/44: Report on the Meeting "High Speed" on Sept. 3, 1940 in Braunschweig (See Supplement) and on Sept. 26 and 27, 1940 in Göttingen.

4. C. Wieselsberger: On the Influence of Wind Tunnel Walls on the Drag, in Particular in the Region of Compressible Flow FB (Research Report) No. 1172.

5. F. Ringleb: Some Aerodynamic Relations for the Wing in Yaw FB No. 1497.

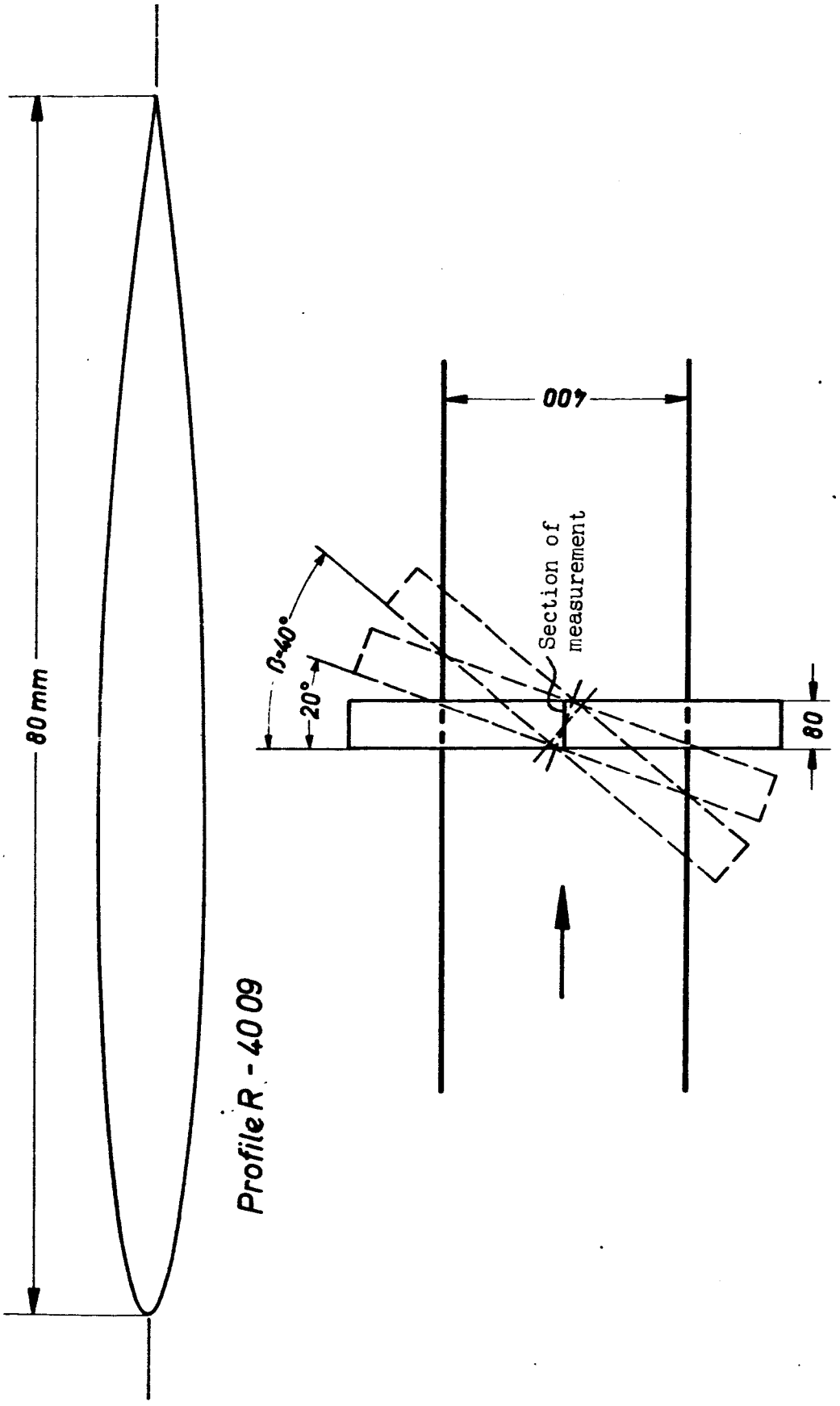

Figure 1.

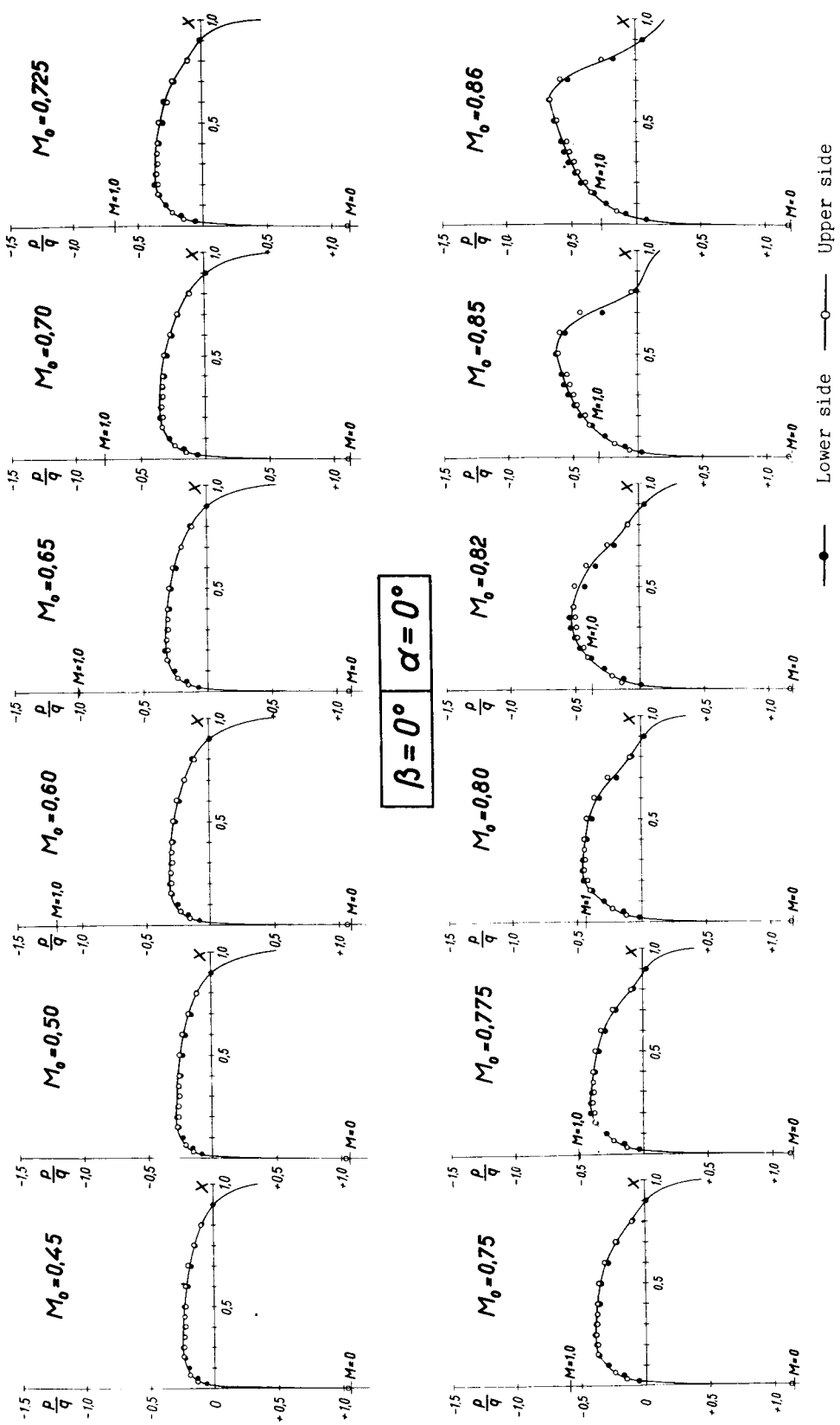
M_0=0,45
M_0=0,50
M_0=0,60
M_0=0,65
M_0=0,70
M_0=0,725
M_0=0,75
M_0=0,775
M_0=0,80
M_0=0,82
M_0=0,85
M_0=0,86
$\beta = 0°$ $\alpha = 0°$
$\frac{p}{q}$
X
M=1,0
M=0
Lower side
Upper side

Figure 2.

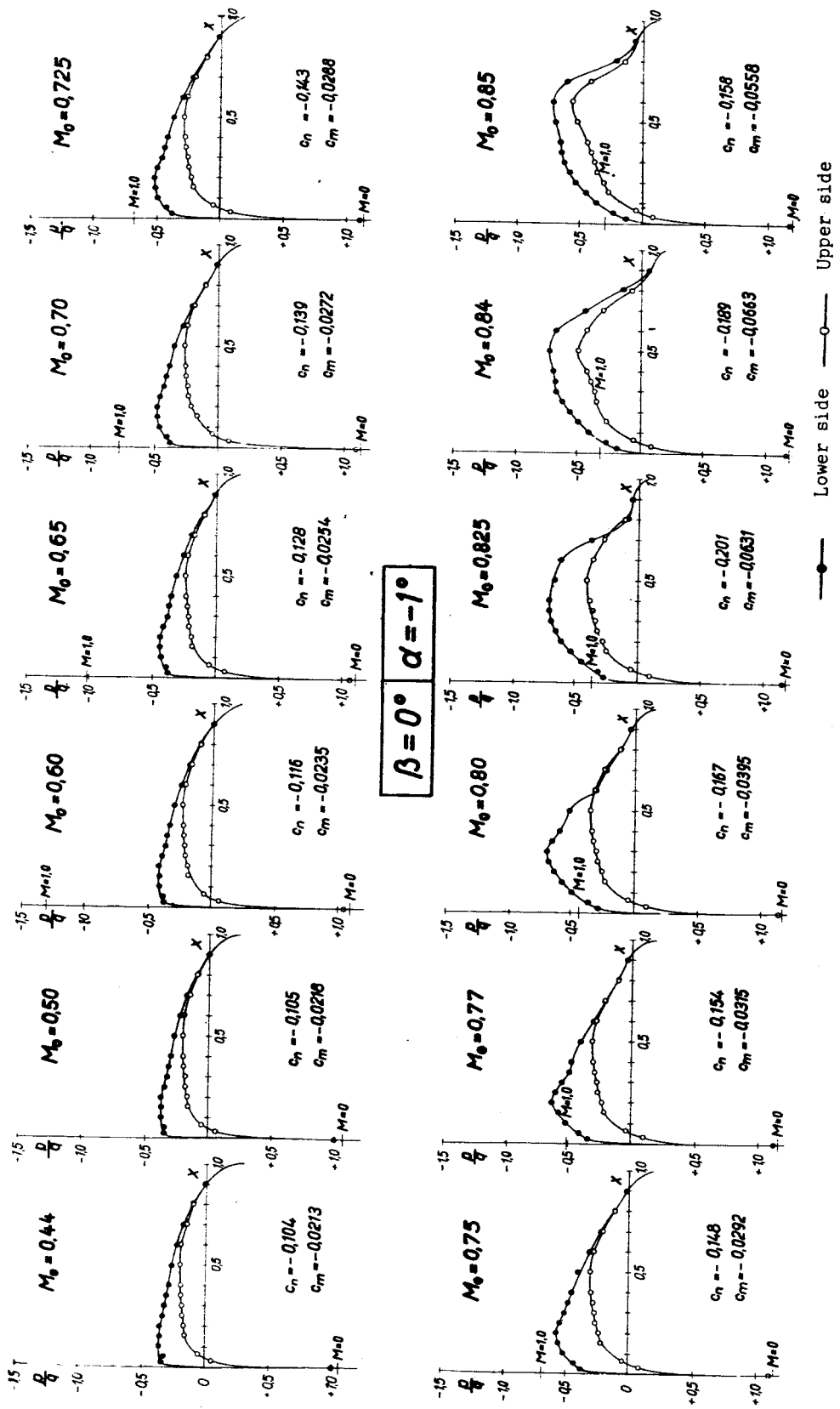
β = 0°
α = -1°
M₀ = 0,44
M₀ = 0,50
M₀ = 0,60
M₀ = 0,65
M₀ = 0,70
M₀ = 0,725
M₀ = 0,75
M₀ = 0,77
M₀ = 0,80
M₀ = 0,825
M₀ = 0,84
M₀ = 0,85
Lower side
Upper side

Figure 3.

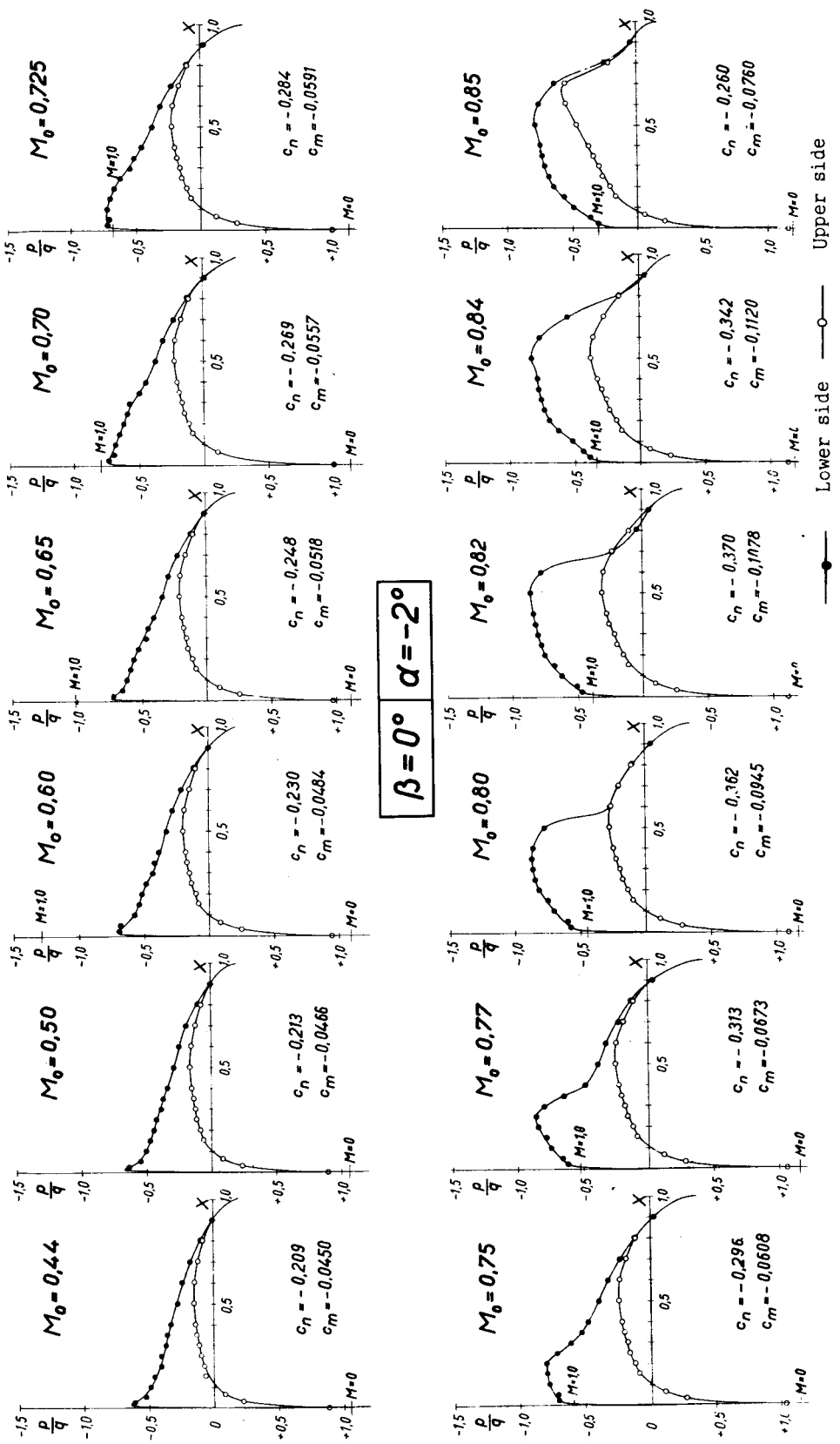
β=0° α=-2°
M₀=0,44
M₀=0,50
M₀=0,60
M₀=0,65
M₀=0,70
M₀=0,725
M₀=0,75
M₀=0,77
M₀=0,80
M₀=0,82
M₀=0,84
M₀=0,85
Lower side
Upper side

Figure 4.

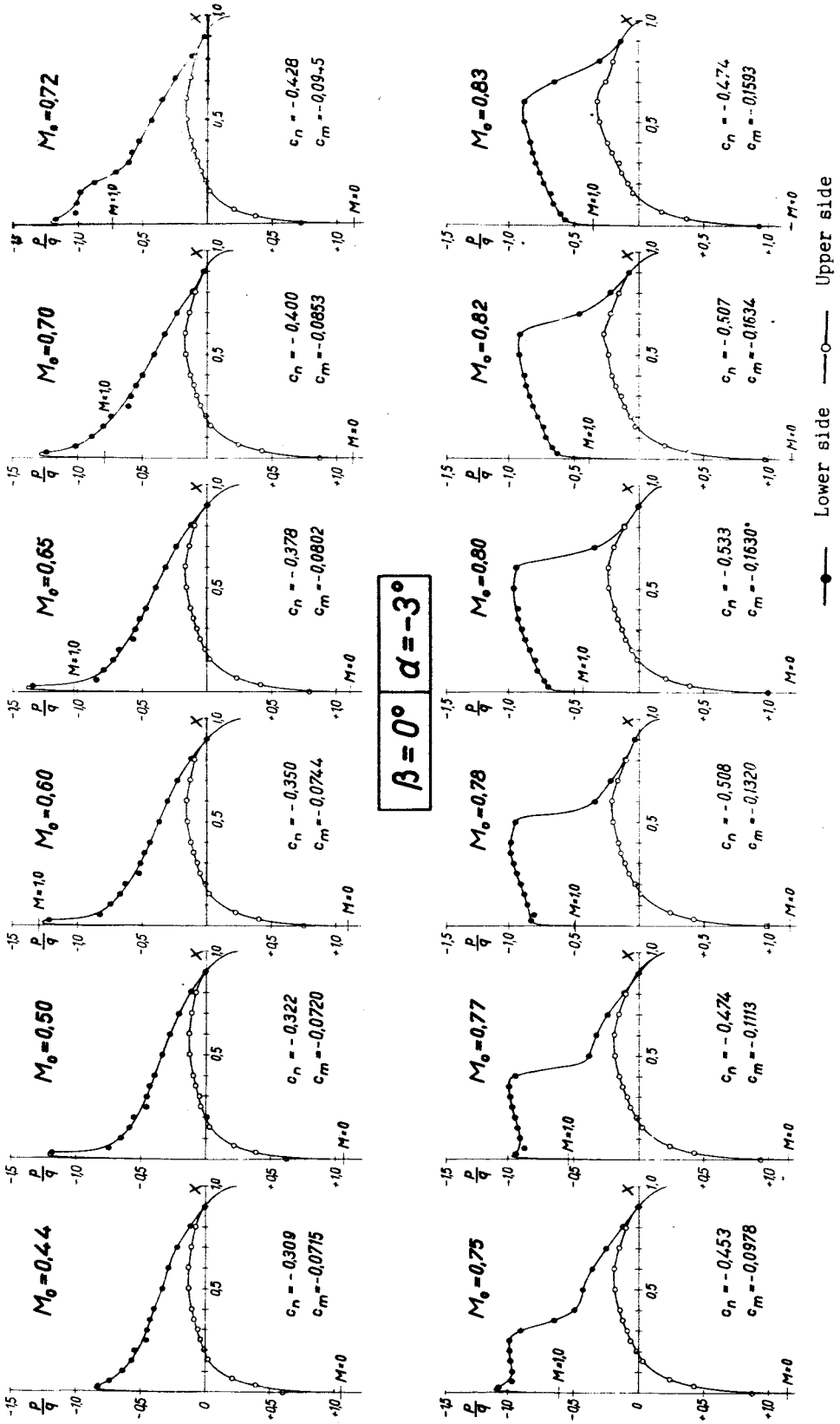
β = 0° α = -3°
M₀=0,44
M₀=0,50
M₀=0,60
M₀=0,65
M₀=0,70
M₀=0,72
M₀=0,75
M₀=0,77
M₀=0,78
M₀=0,80
M₀=0,82
M₀=0,83
Lower side
Upper side

Figure 5.

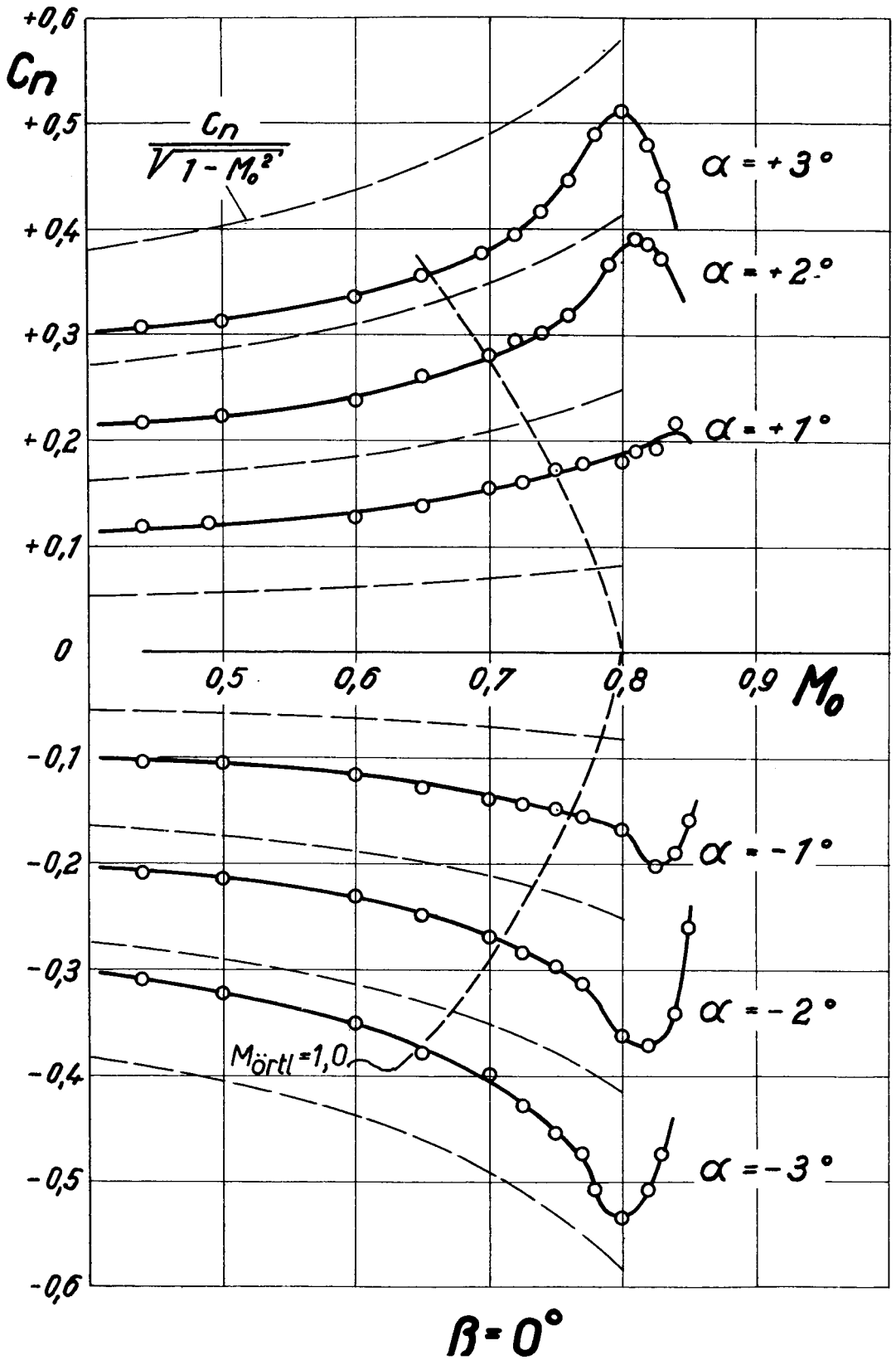
+0,6
Cn
+0,5
+0,4
+0,3
+0,2
+0,1
0
-0,1
-0,2
-0,3
-0,4
-0,5
-0,6
Cn / √1 - M0²
α = +3°
α = +2°
α = +1°
α = -1°
α = -2°
α = -3°
0,5
0,6
0,7
0,8
0,9
M0
Mörtl = 1,0
β = 0°

Figure 6.

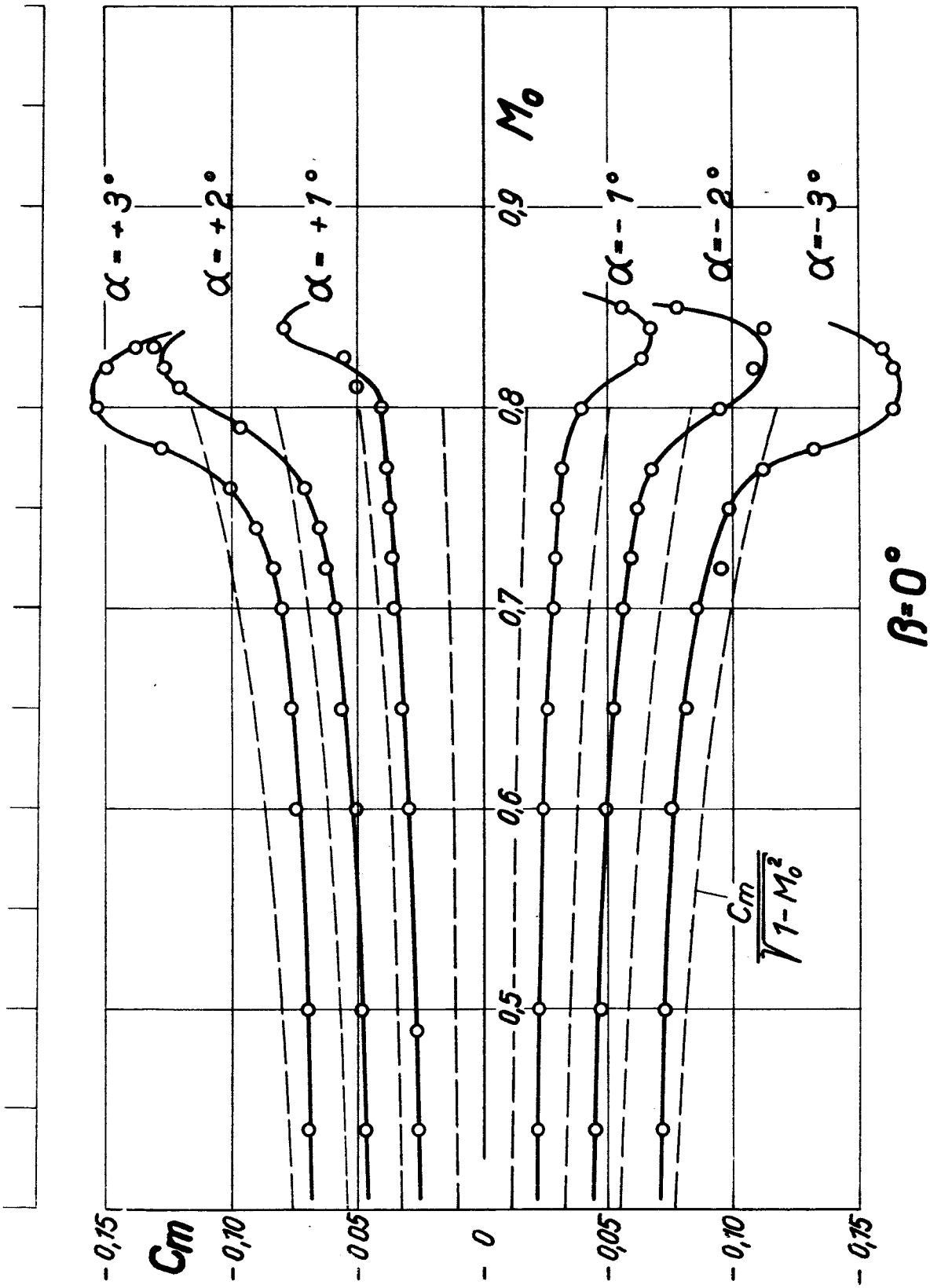
α = +3°
α = +2°
α = +1°
α = -1°
α = -2°
α = -3°
M₀
0,9
0,8
0,7
0,6
0,5
Cm
-0,15
-0,10
-0,05
0
-0,05
-0,10
-0,15
Cm / √(1-M₀²)
β=0°

Figure 7.

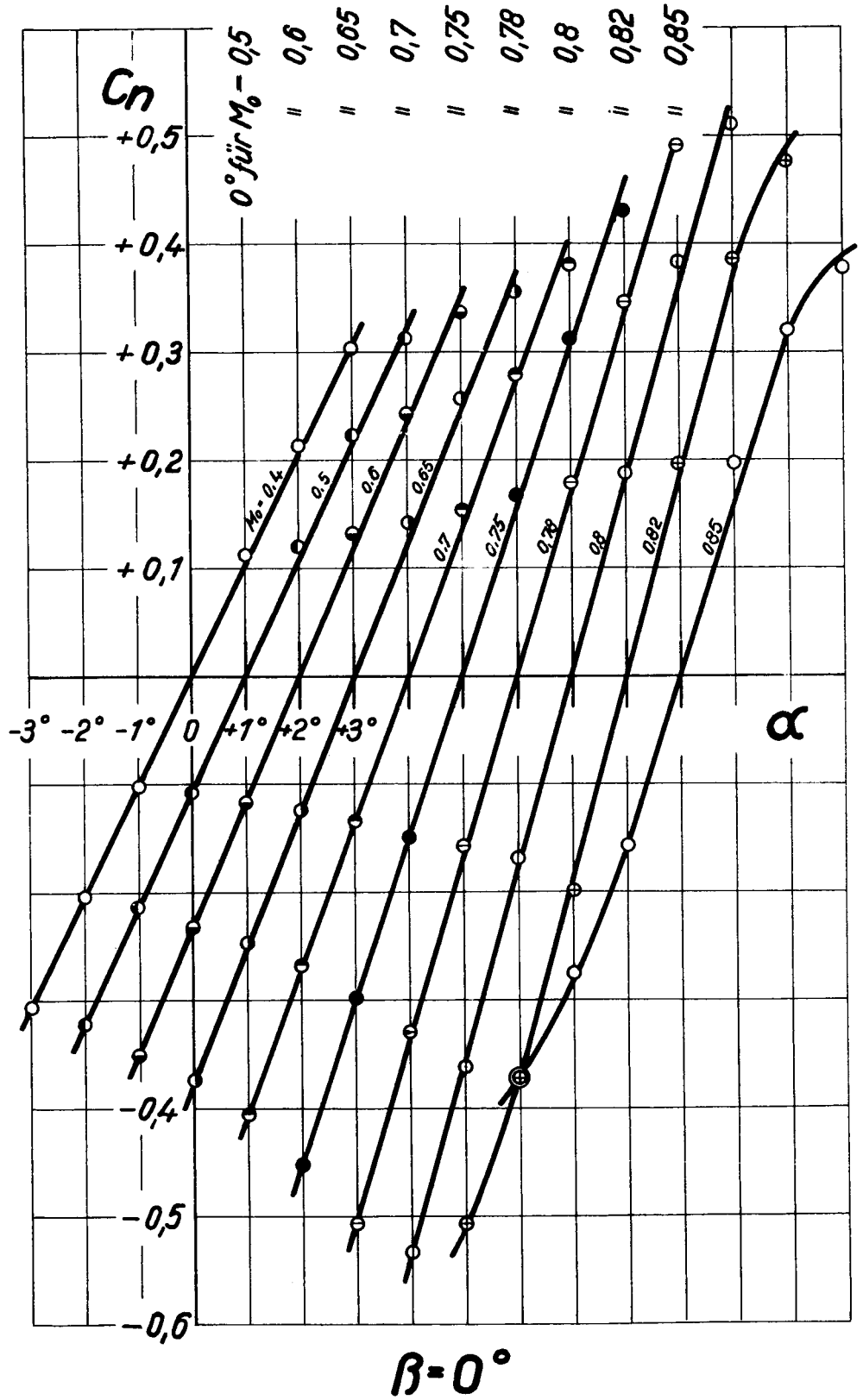
Cn
+0,5
+0,4
+0,3
+0,2
+0,1
-0,4
-0,5
-0,6
0° für M₀ - 0,5 = 0,6 = 0,65 = 0,7 = 0,75 = 0,78 = 0,8 = 0,82 = 0,85
M₀ = 0,4
0,5
0,6
0,65
0,7
0,75
0,78
0,8
0,82
0,85
-3° -2° -1° 0 +1° +2° +3°
α
β = 0°

Figure 8.

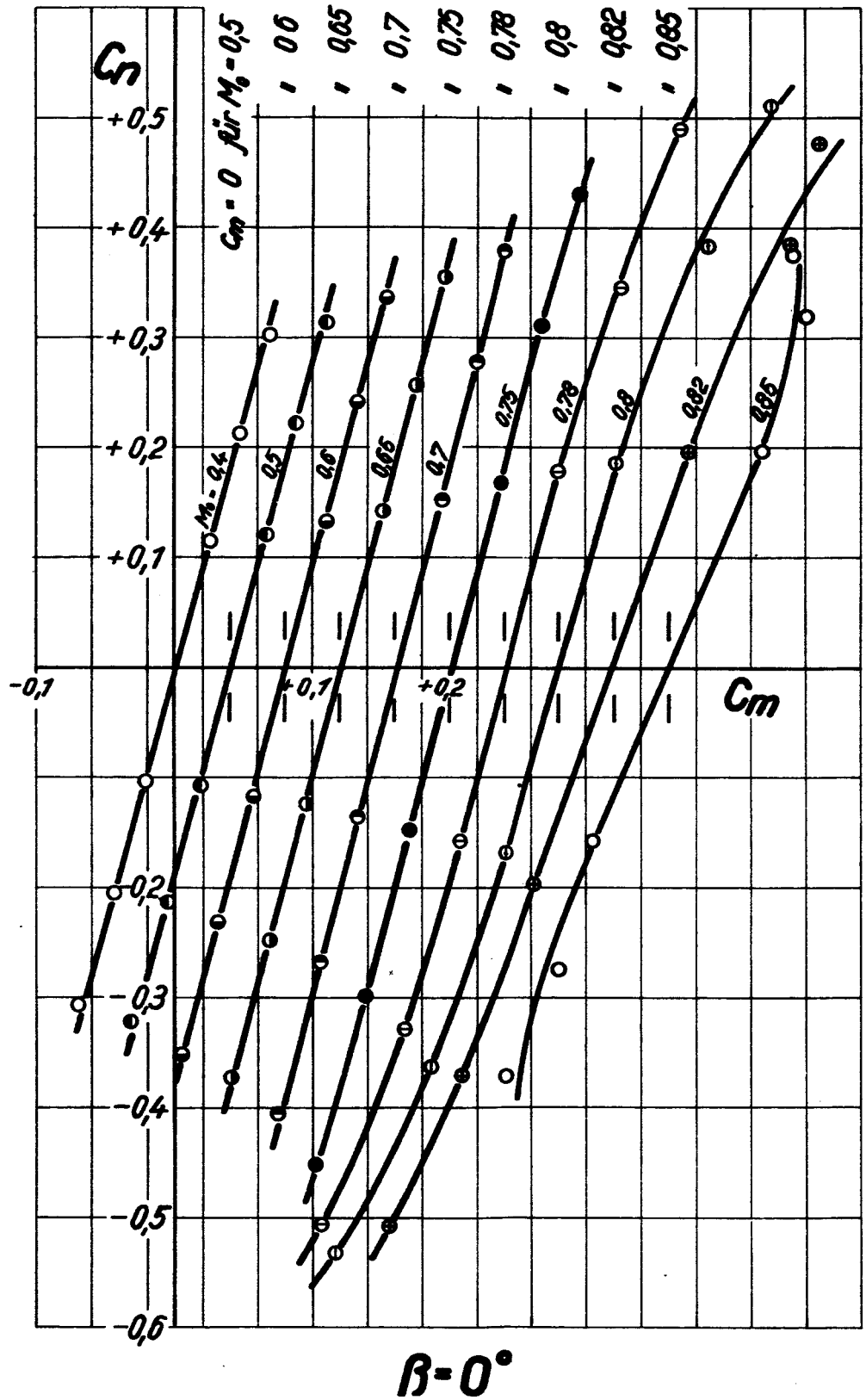
Cn
+0,5
+0,4
+0,3
+0,2
+0,1
-0,1
+0,1
+0,2
Cm
-0,2
-0,3
-0,4
-0,5
-0,6
Cm = 0 für Ma = 0,5
0,6
0,65
0,7
0,75
0,78
0,8
0,82
0,85
Ma = 0,4
0,5
0,6
0,65
0,7
0,75
0,78
0,8
0,82
0,85
β = 0°

Figure 9.

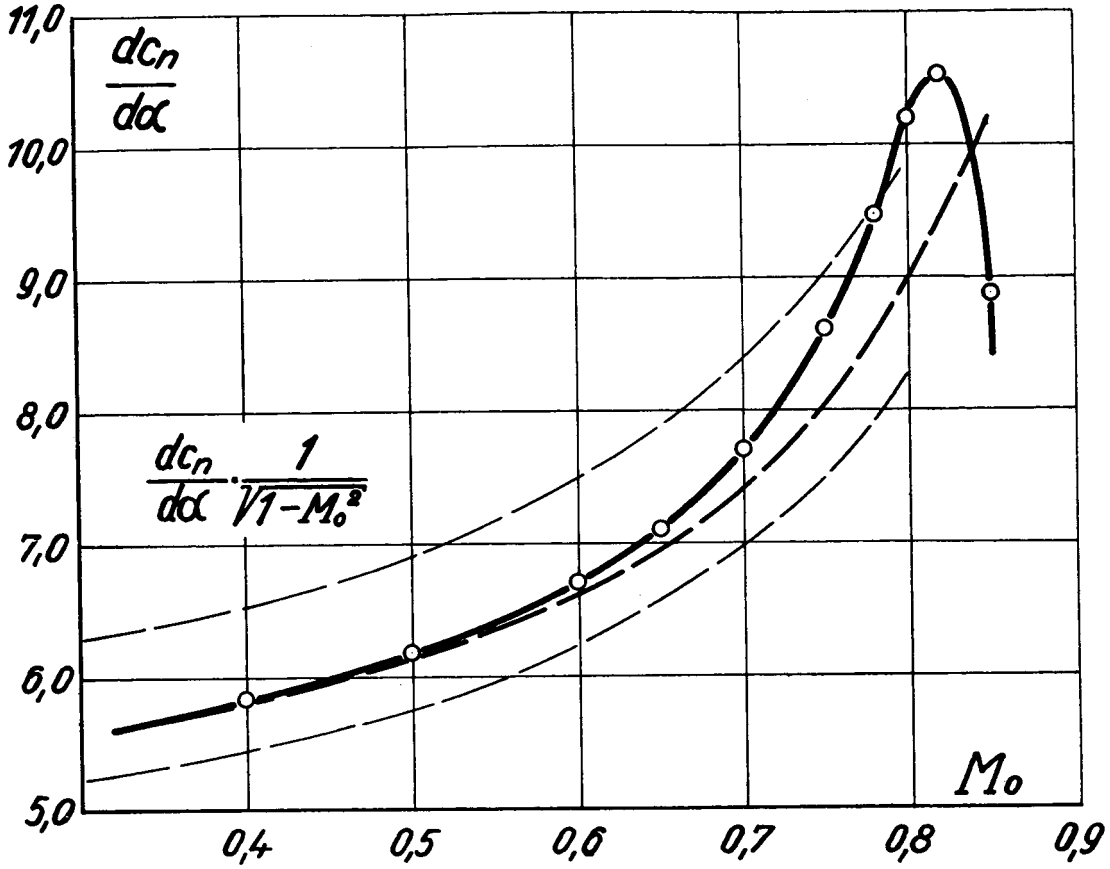
11,0
10,0
9,0
8,0
7,0
6,0
5,0
$\frac{dc_n}{d\alpha}$
$\frac{dc_n}{d\alpha} \cdot \frac{1}{\sqrt{1-M_0^2}}$
0,4
0,5
0,6
0,7
0,8
0,9
M_0

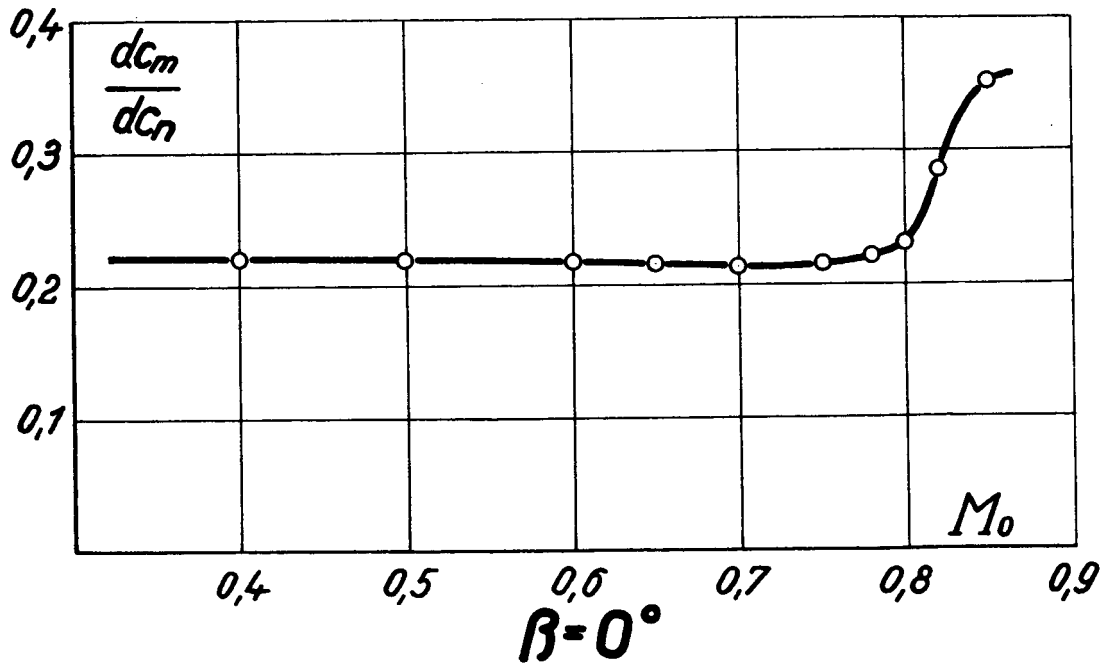
0,4
0,3
0,2
0,1
$\frac{dc_m}{dc_n}$
0,4
0,5
0,6
0,7
0,8
0,9
M_0
$\beta = 0°$

Figure 10.

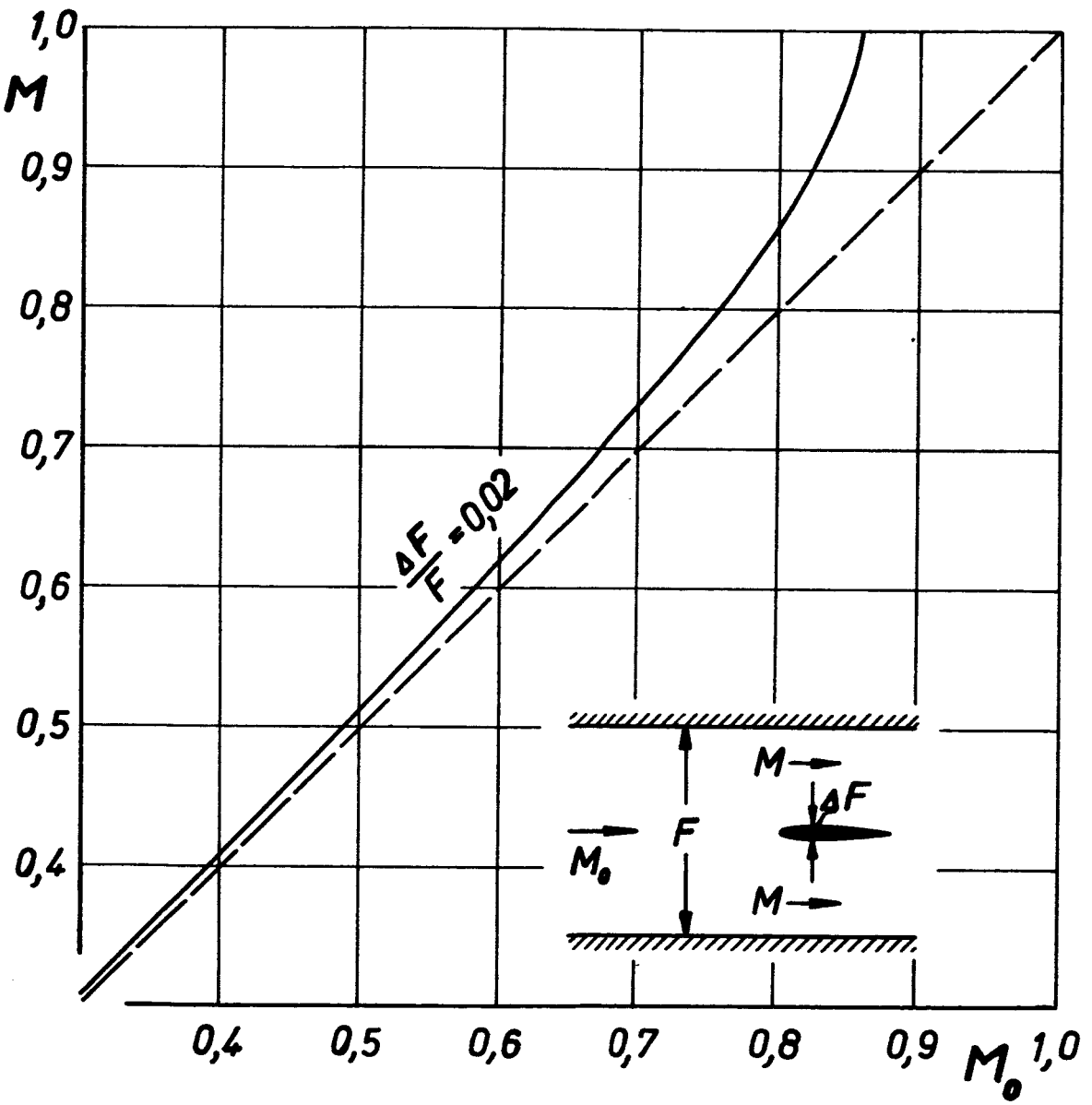

Figure 11.

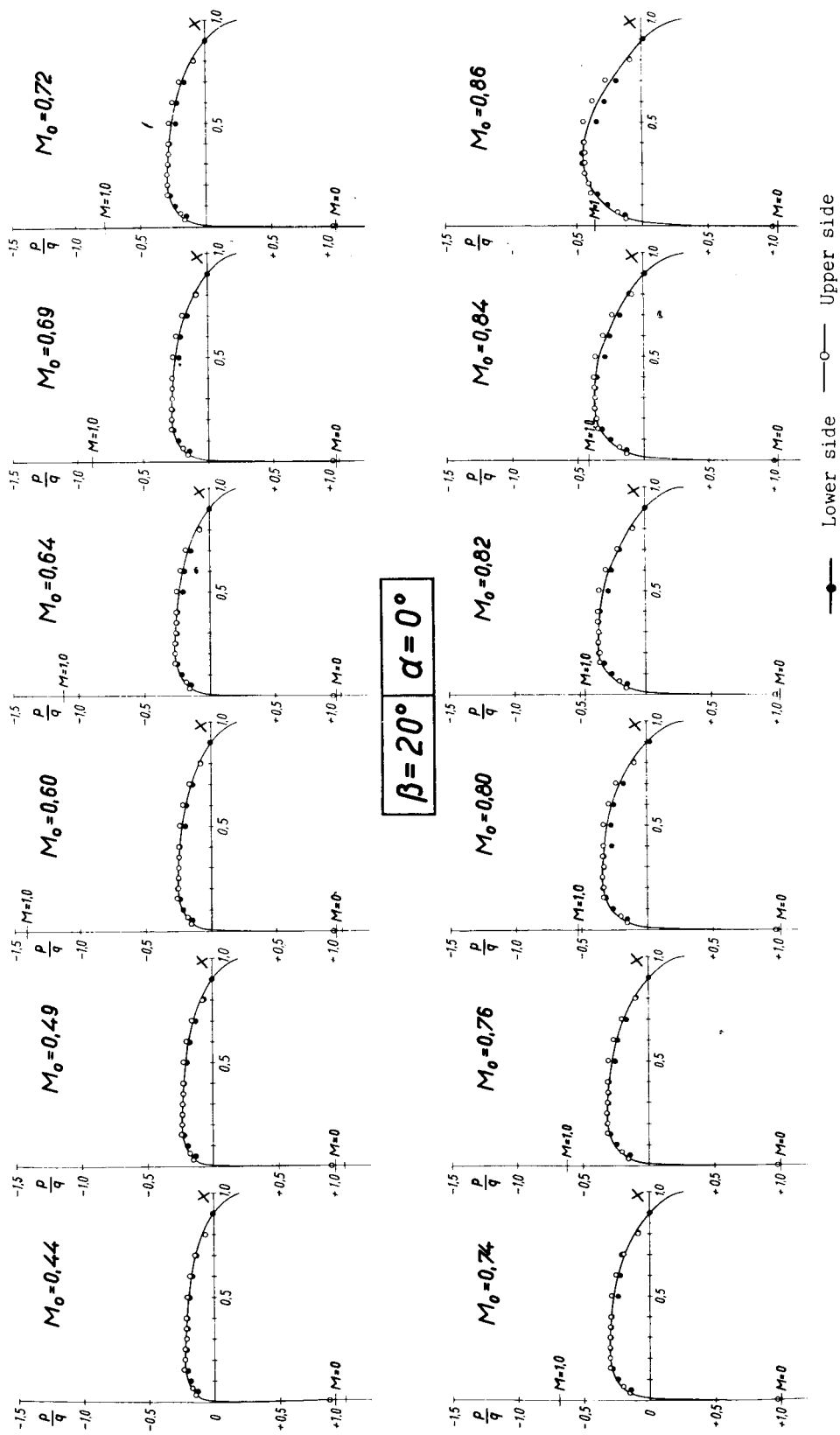
β=20° α=0°
M₀=0,44
M₀=0,49
M₀=0,60
M₀=0,64
M₀=0,69
M₀=0,72
M₀=0,74
M₀=0,76
M₀=0,80
M₀=0,82
M₀=0,84
M₀=0,86
Lower side
Upper side

Figure 12.

Fig. 13

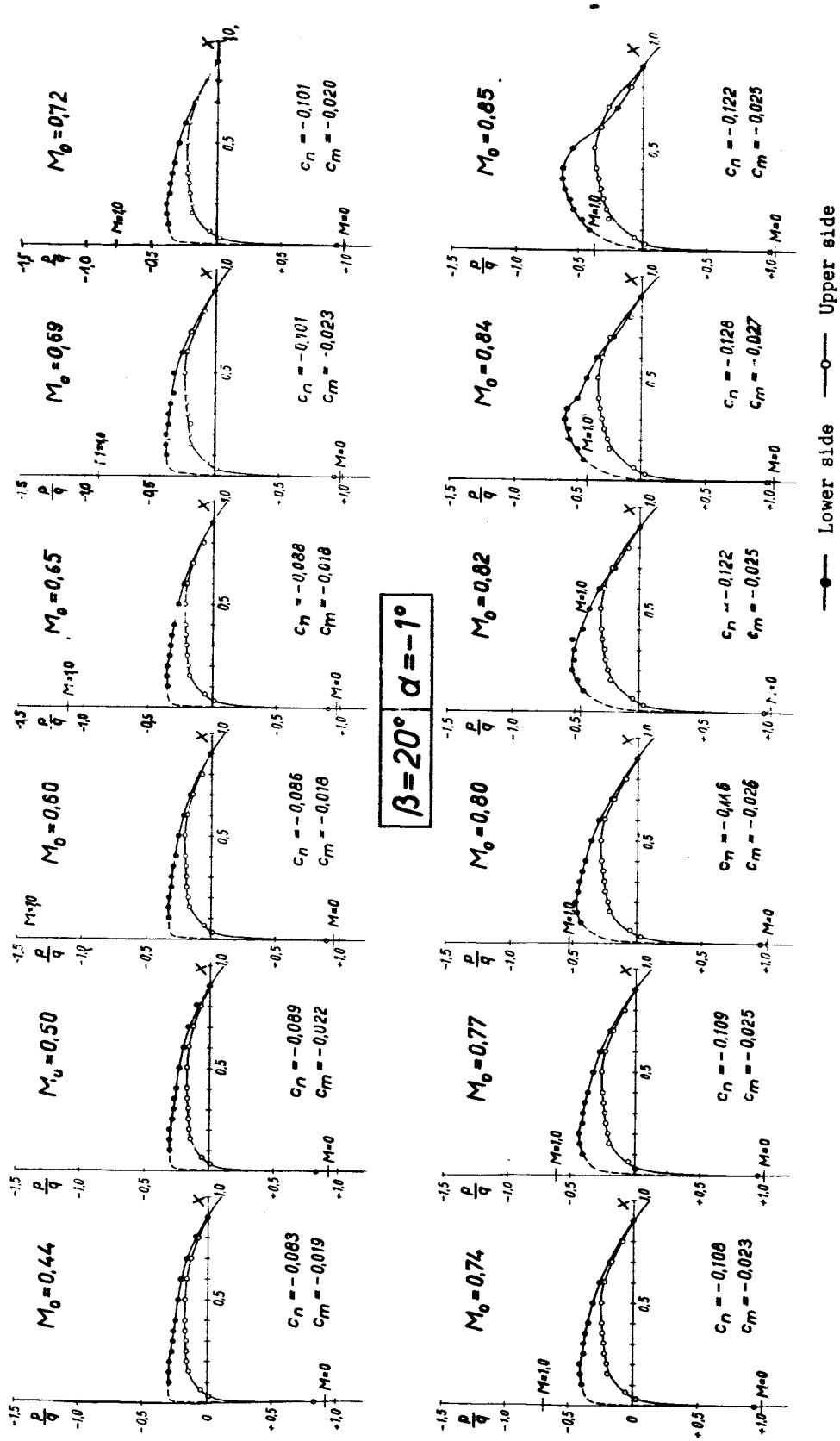

Figure 13.

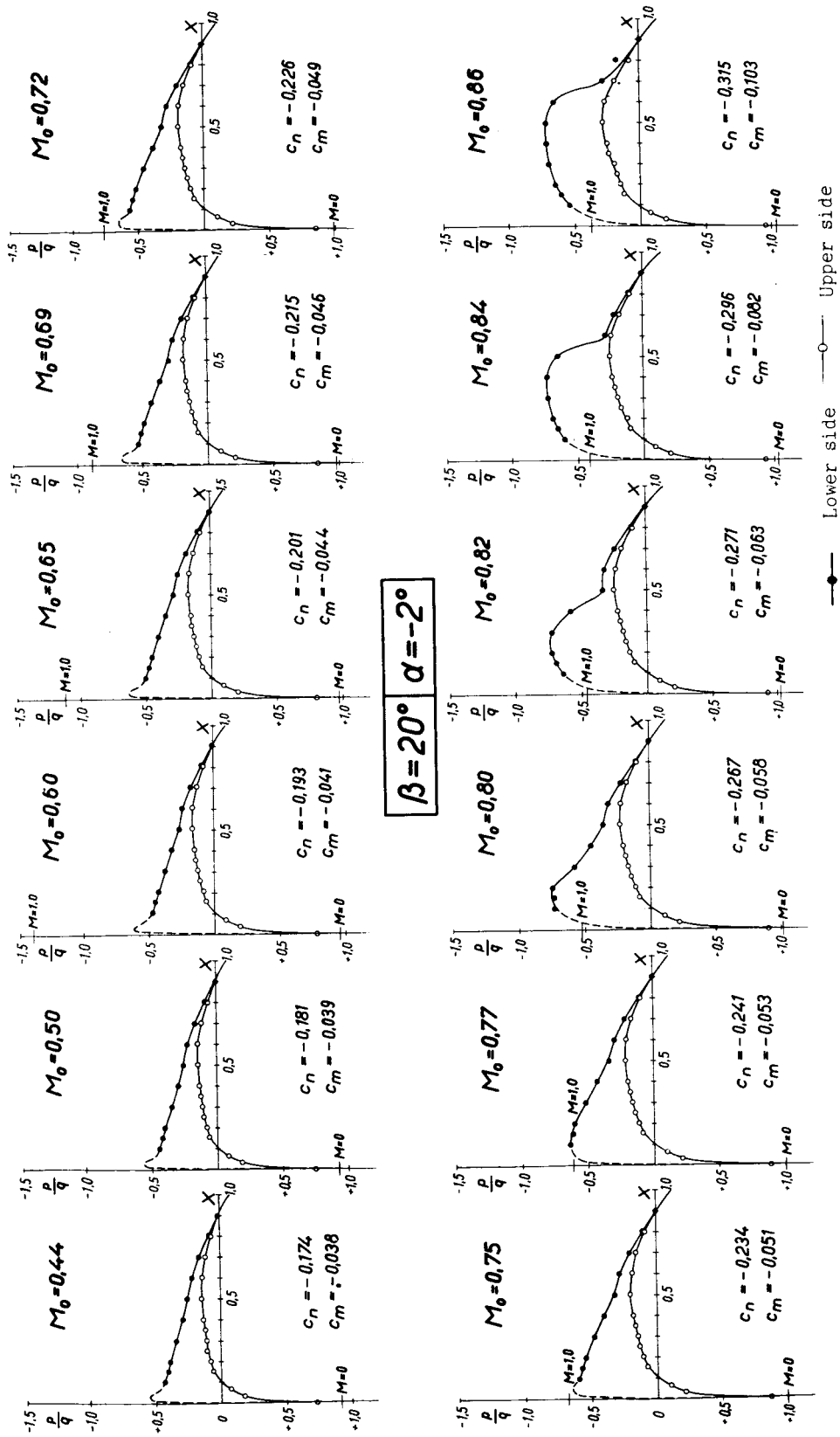
β=20° α=-2°
M₀=0,44
M₀=0,50
M₀=0,60
M₀=0,65
M₀=0,69
M₀=0,72
M₀=0,75
M₀=0,77
M₀=0,80
M₀=0,82
M₀=0,84
M₀=0,86
Lower side
Upper side

Figure 14.

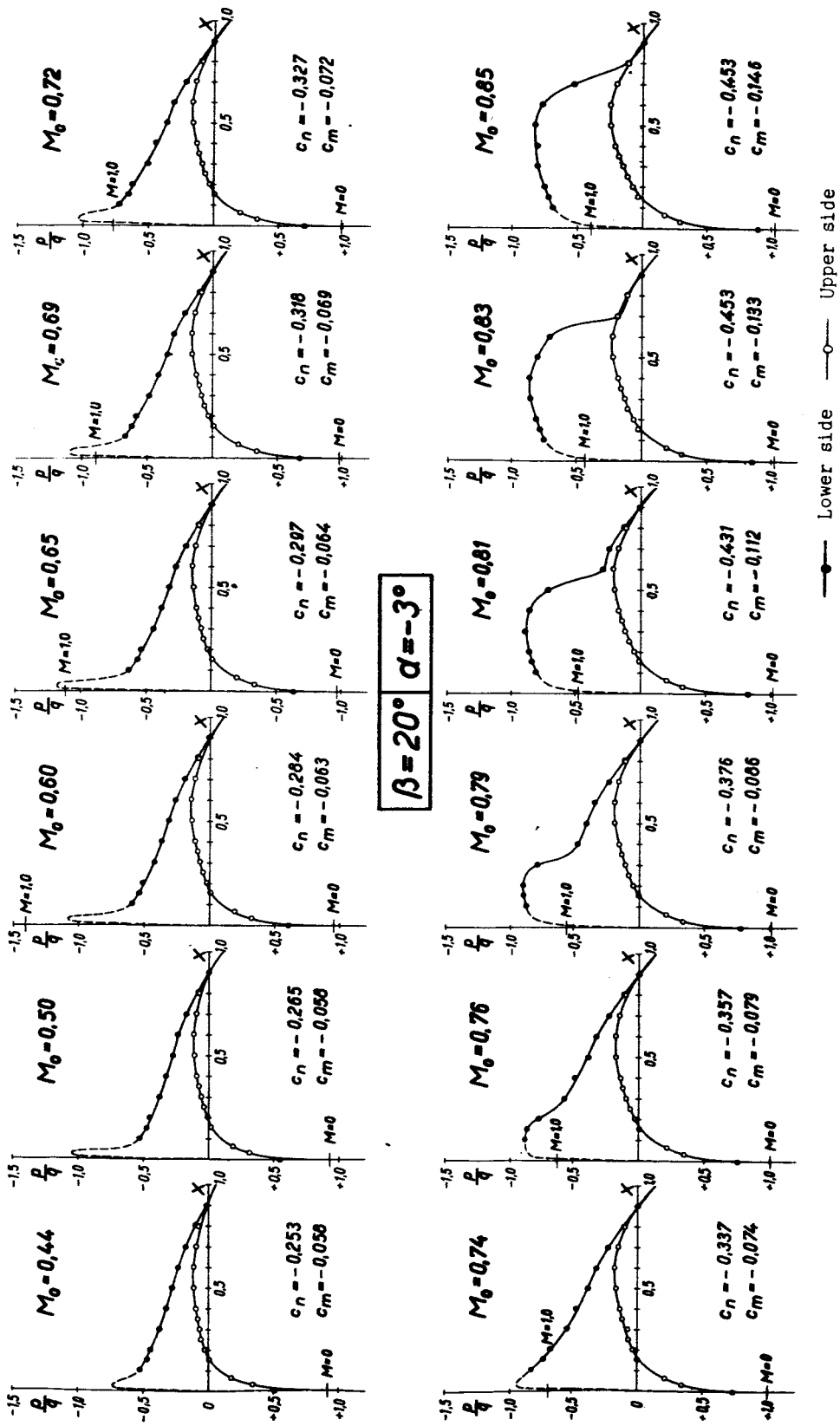
β=20° α=-3°
M₀=0,44
M₀=0,50
M₀=0,60
M₀=0,65
M₀=0,69
M₀=0,72
M₀=0,74
M₀=0,76
M₀=0,79
M₀=0,81
M₀=0,83
M₀=0,85
Lower side
Upper side

Figure 15.

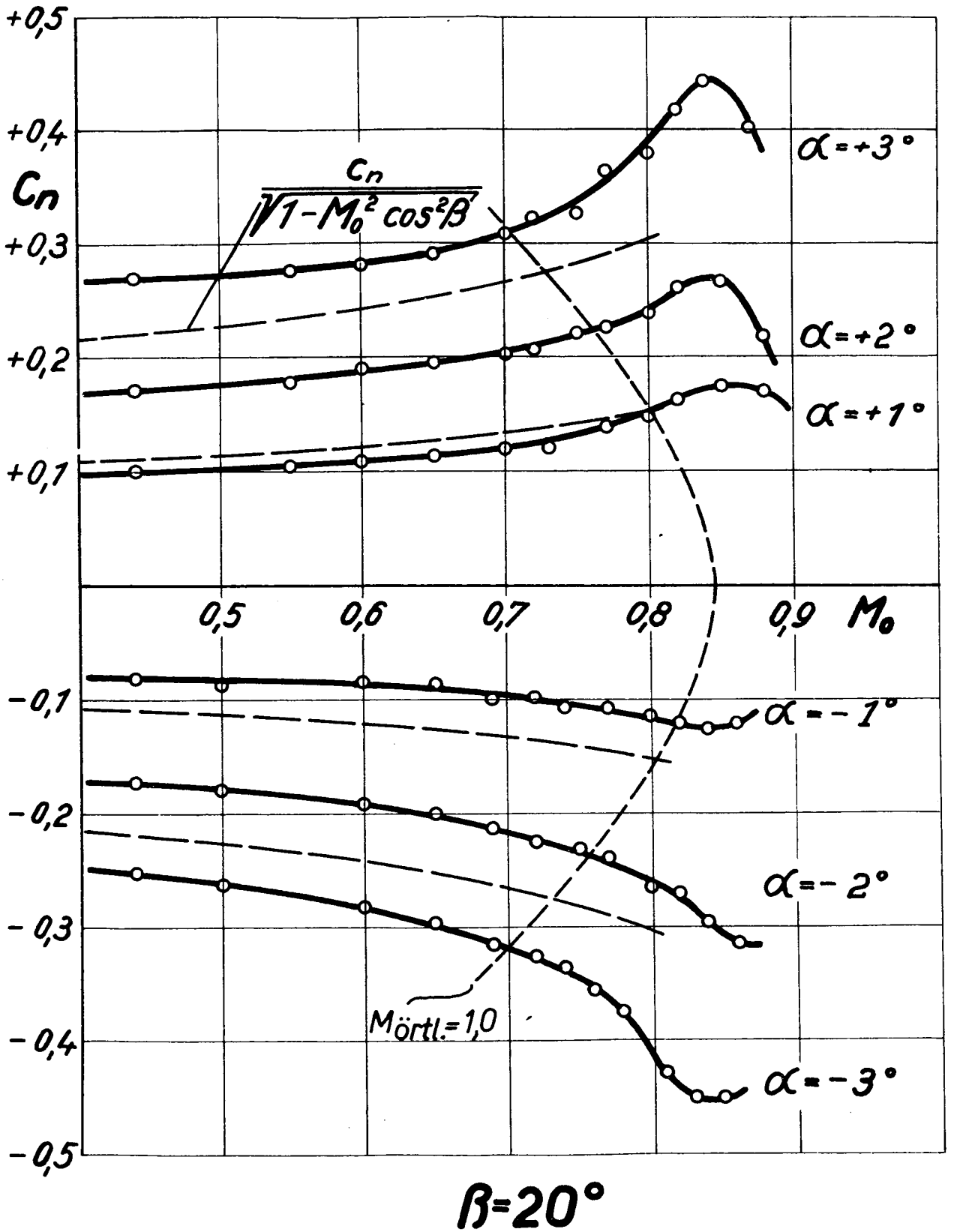
+0,5
+0,4
Cn
+0,3
+0,2
+0,1
Cn / √1-M0² cos²β
α=+3°
α=+2°
α=+1°
0,5
0,6
0,7
0,8
0,9
M0
-0,1
-0,2
-0,3
-0,4
-0,5
α=-1°
α=-2°
α=-3°
Mörtl.=1,0
β=20°

Figure 16.

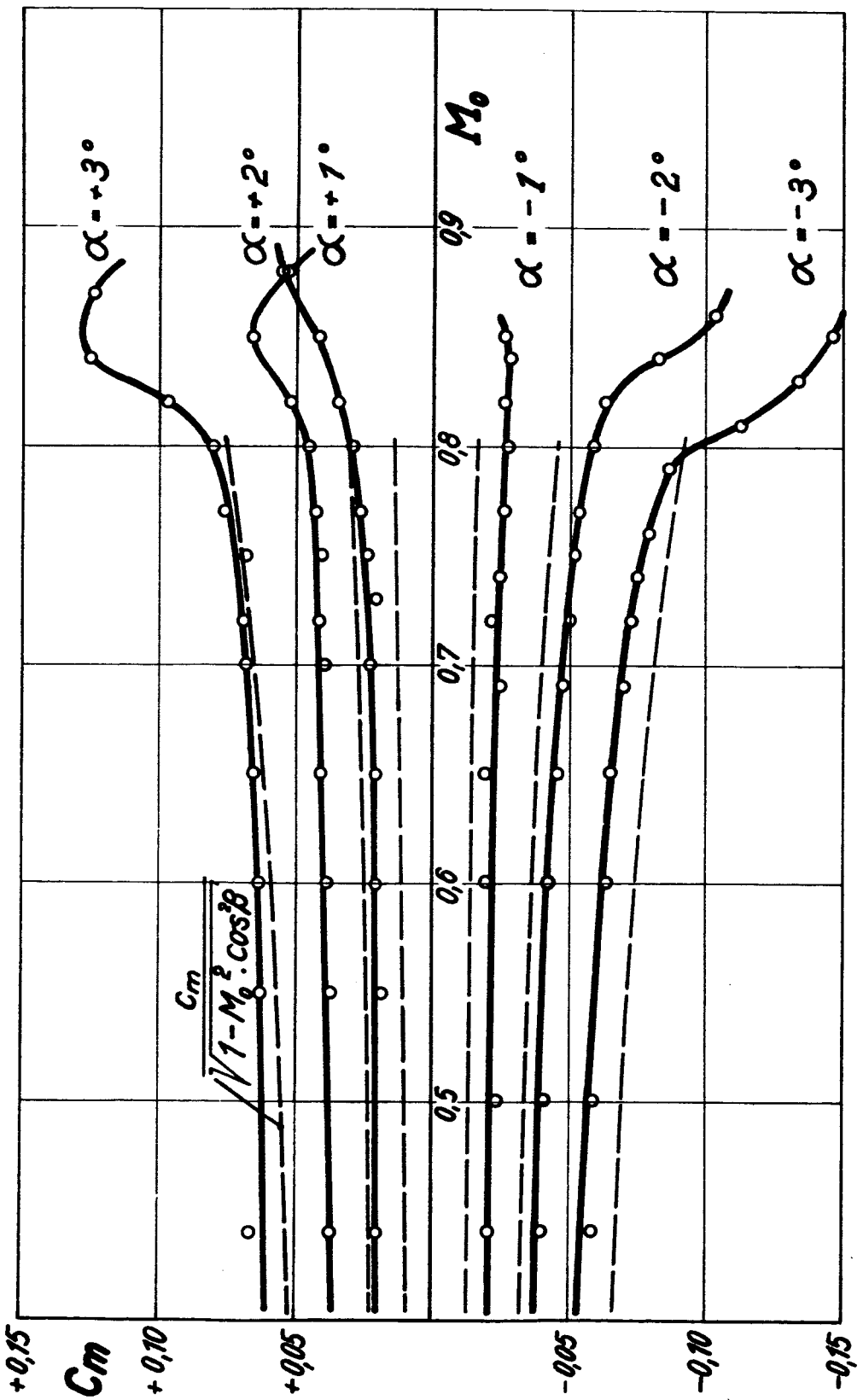
α = +3°
α = +2°
α = +1°
α = -1°
α = -2°
α = -3°
M₀
0,9
0,8
0,7
0,6
0,5
β=20°
Cm
+0,15
+0,10
+0,05
-0,05
-0,10
-0,15
Cm / √(1-M₀²·cos²β)

Figure 17.

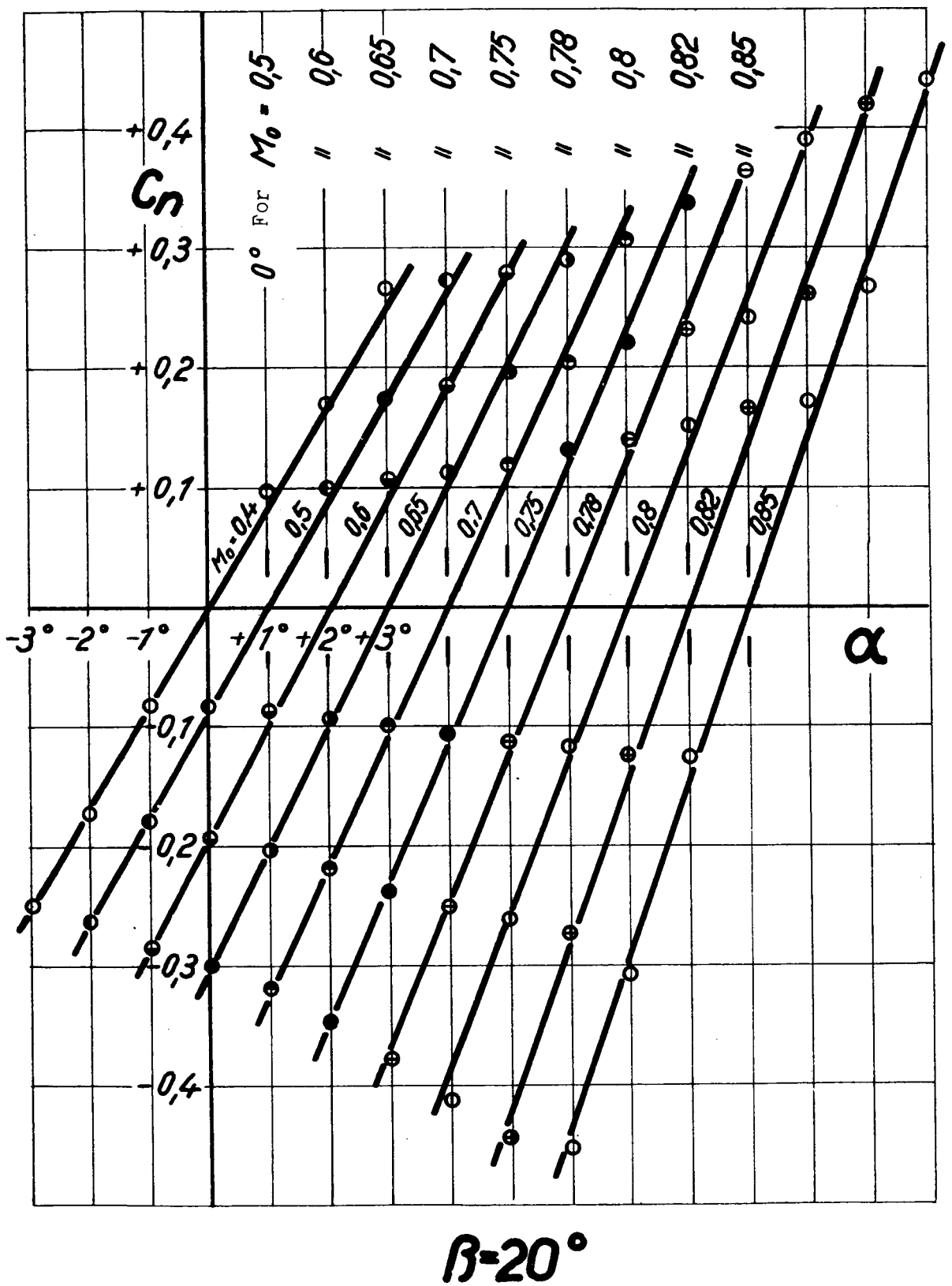
For M_o = 0,5 0,6 0,65 0,7 0,75 0,78 0,8 0,82 0,85
0°
C_n
+0,4
+0,3
+0,2
+0,1
-0,1
-0,2
-0,3
-0,4
M_o=0,4 0,5 0,6 0,65 0,7 0,75 0,78 0,8 0,82 0,85
-3° -2° -1° +1° +2° +3°
α
β=20°

Figure 18.

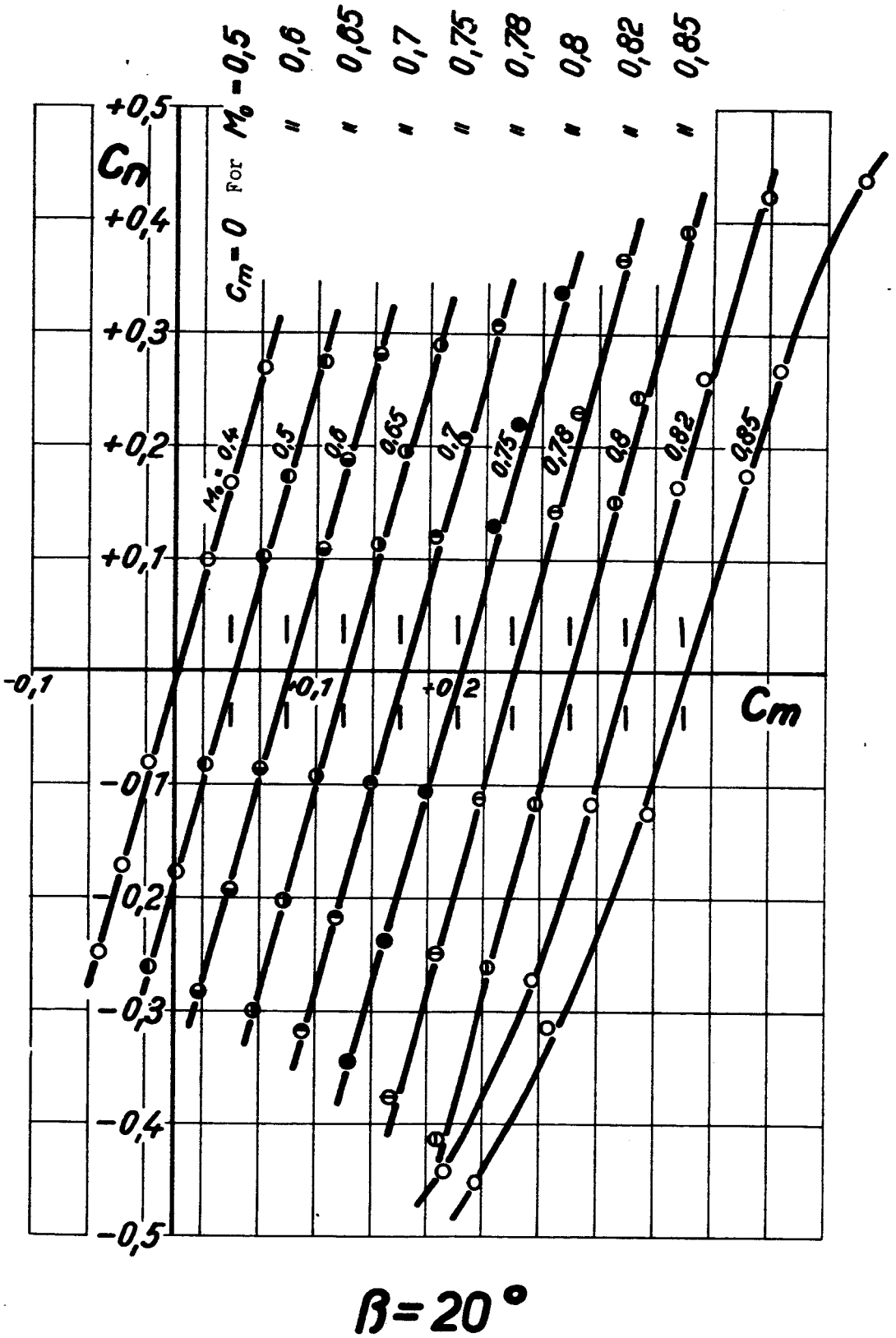
Cn
Cm
For Cm = 0
M₀ = 0,5
" 0,6
" 0,65
" 0,7
" 0,75
" 0,78
" 0,8
" 0,82
" 0,85
+0,5
+0,4
+0,3
+0,2
+0,1
-0,1
-0,2
-0,3
-0,4
-0,5
+0,1
+0,2
M₀: 0,4
0,5
0,6
0,65
0,7
0,75
0,78
0,8
0,82
0,85
β = 20°

Figure 19.

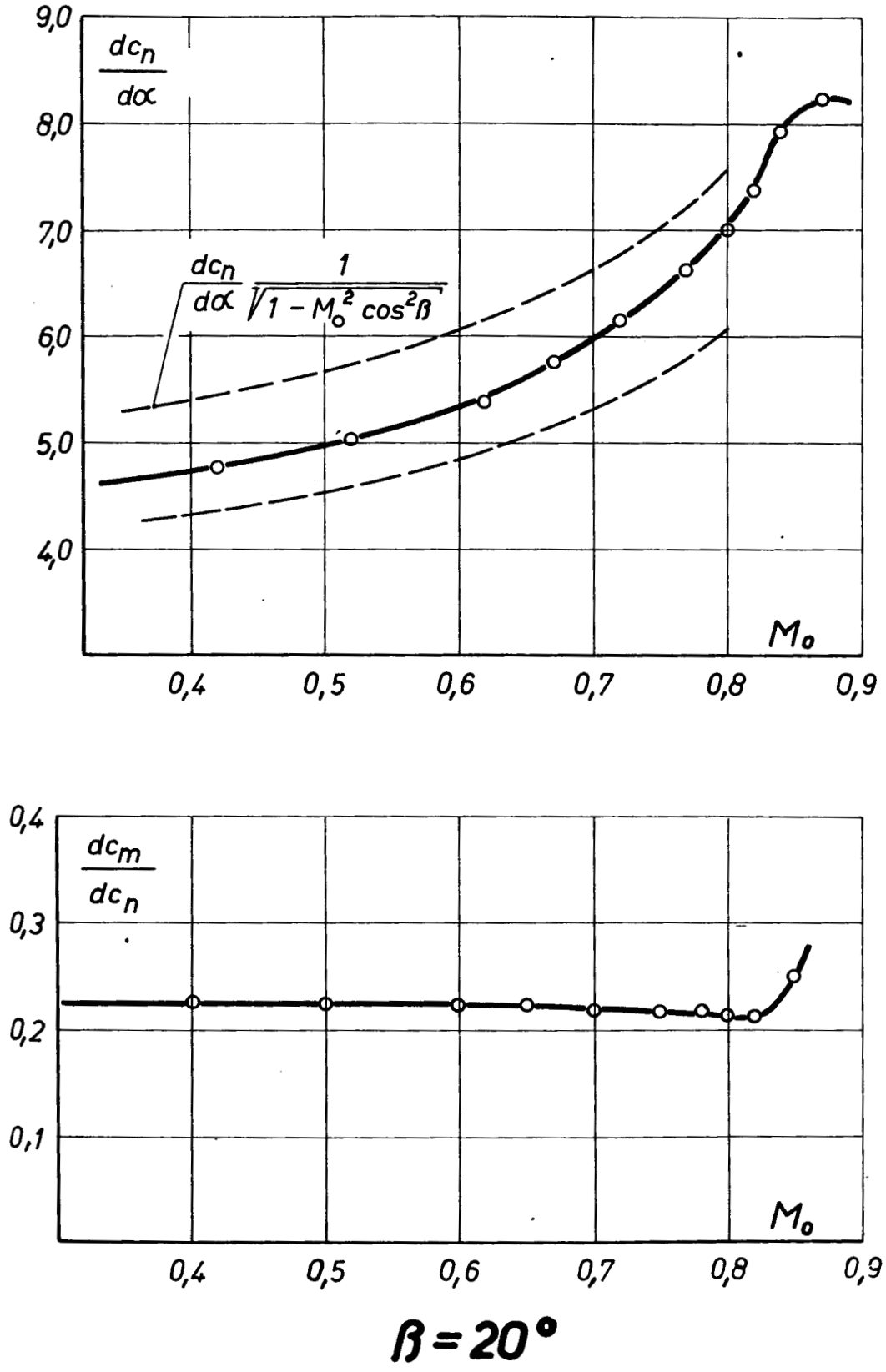
9,0
8,0
7,0
6,0
5,0
4,0
$\frac{dc_n}{d\alpha}$
$\frac{dc_n}{d\alpha}\frac{1}{\sqrt{1-M_o^2\cos^2\beta}}$
M_o
0,4
0,5
0,6
0,7
0,8
0,9
0,4
0,3
0,2
0,1
$\frac{dc_m}{dc_n}$
M_o
0,4
0,5
0,6
0,7
0,8
0,9
$\beta = 20°$

Figure 20.

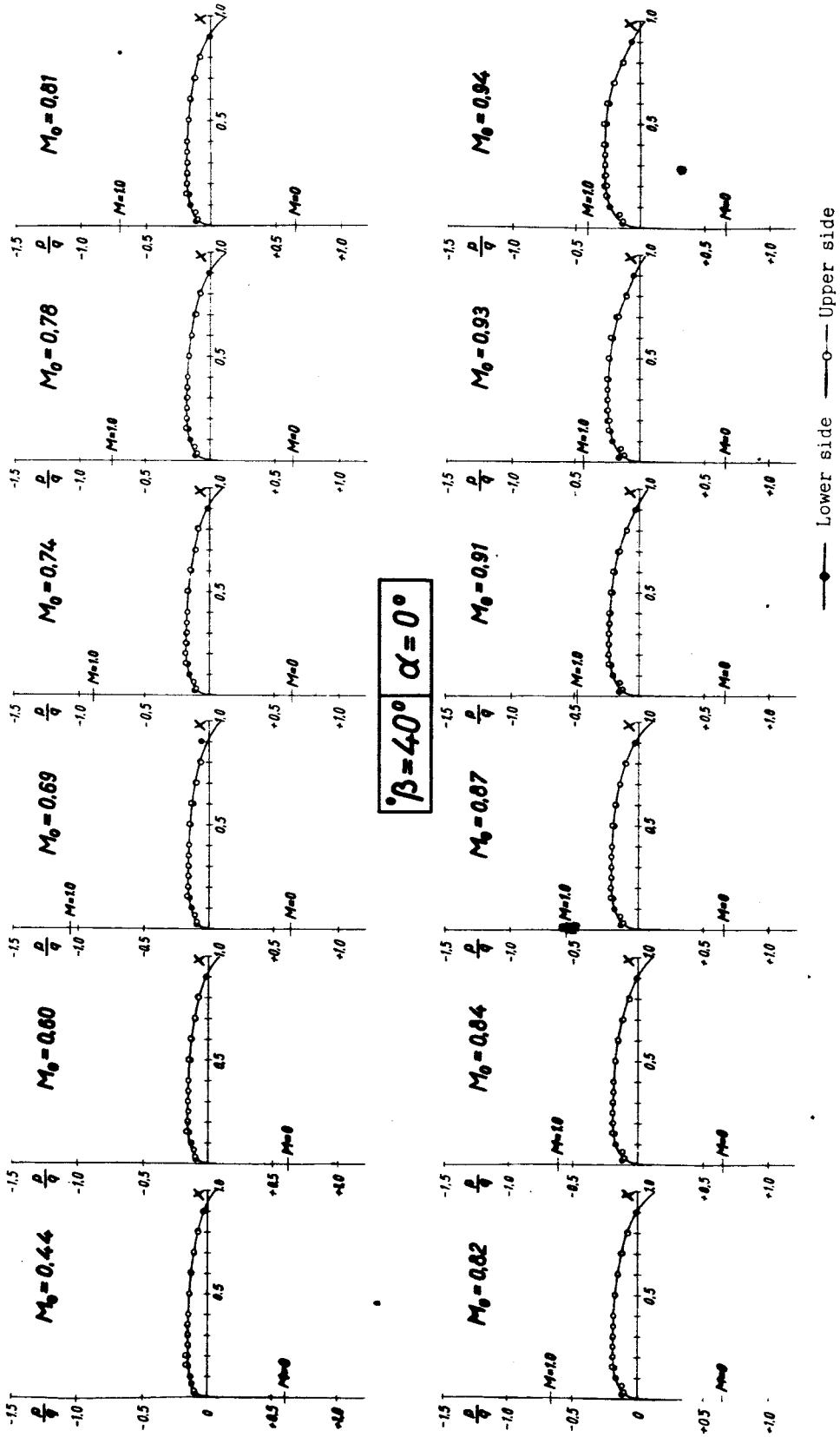
$M_0 = 0.44$
$M_0 = 0.60$
$M_0 = 0.69$
$M_0 = 0.74$
$M_0 = 0.78$
$M_0 = 0.81$
$M_0 = 0.82$
$M_0 = 0.84$
$M_0 = 0.87$
$M_0 = 0.91$
$M_0 = 0.93$
$M_0 = 0.94$
$\beta = 40°$
$\alpha = 0°$
Lower side
Upper side

Figure 21.

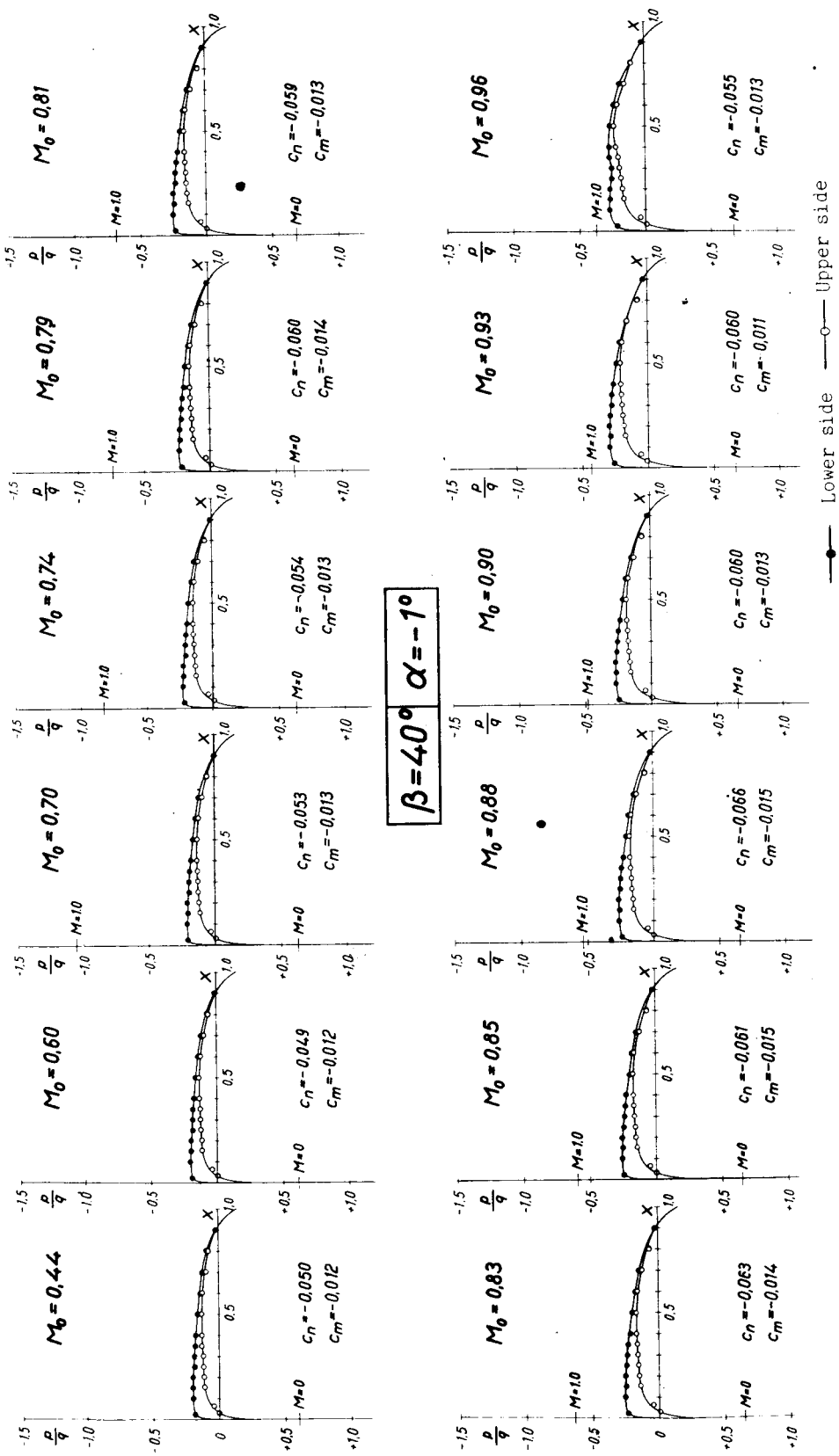
β=40° α=-1°
M₀=0,44
M₀=0,60
M₀=0,70
M₀=0,74
M₀=0,79
M₀=0,81
M₀=0,83
M₀=0,85
M₀=0,88
M₀=0,90
M₀=0,93
M₀=0,96
Lower side
Upper side

Figure 22.

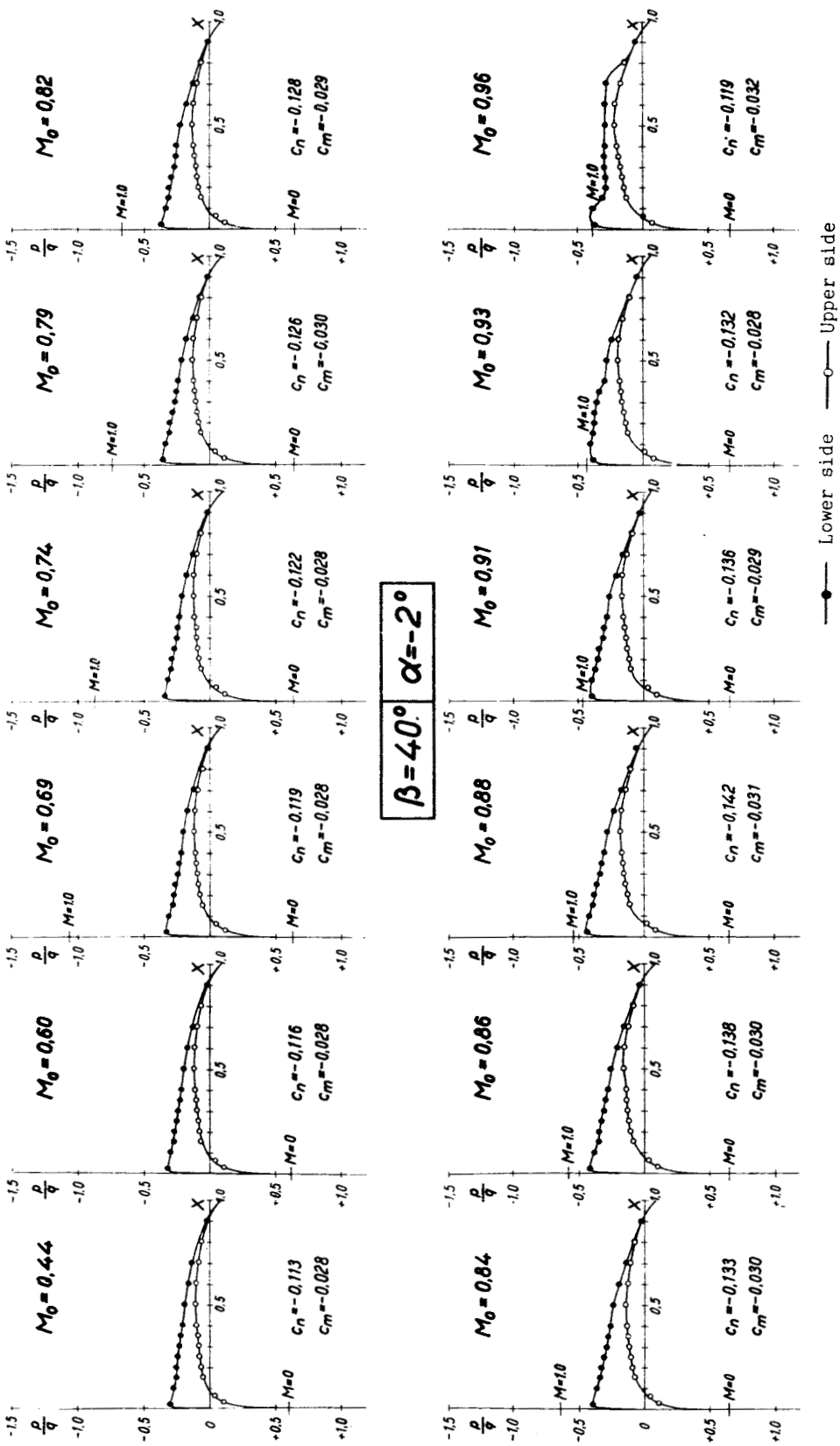
β=40° α=-2°
M₀=0,44
M₀=0,60
M₀=0,69
M₀=0,74
M₀=0,79
M₀=0,82
M₀=0,84
M₀=0,86
M₀=0,88
M₀=0,91
M₀=0,93
M₀=0,96
Lower side
Upper side

Figure 23.

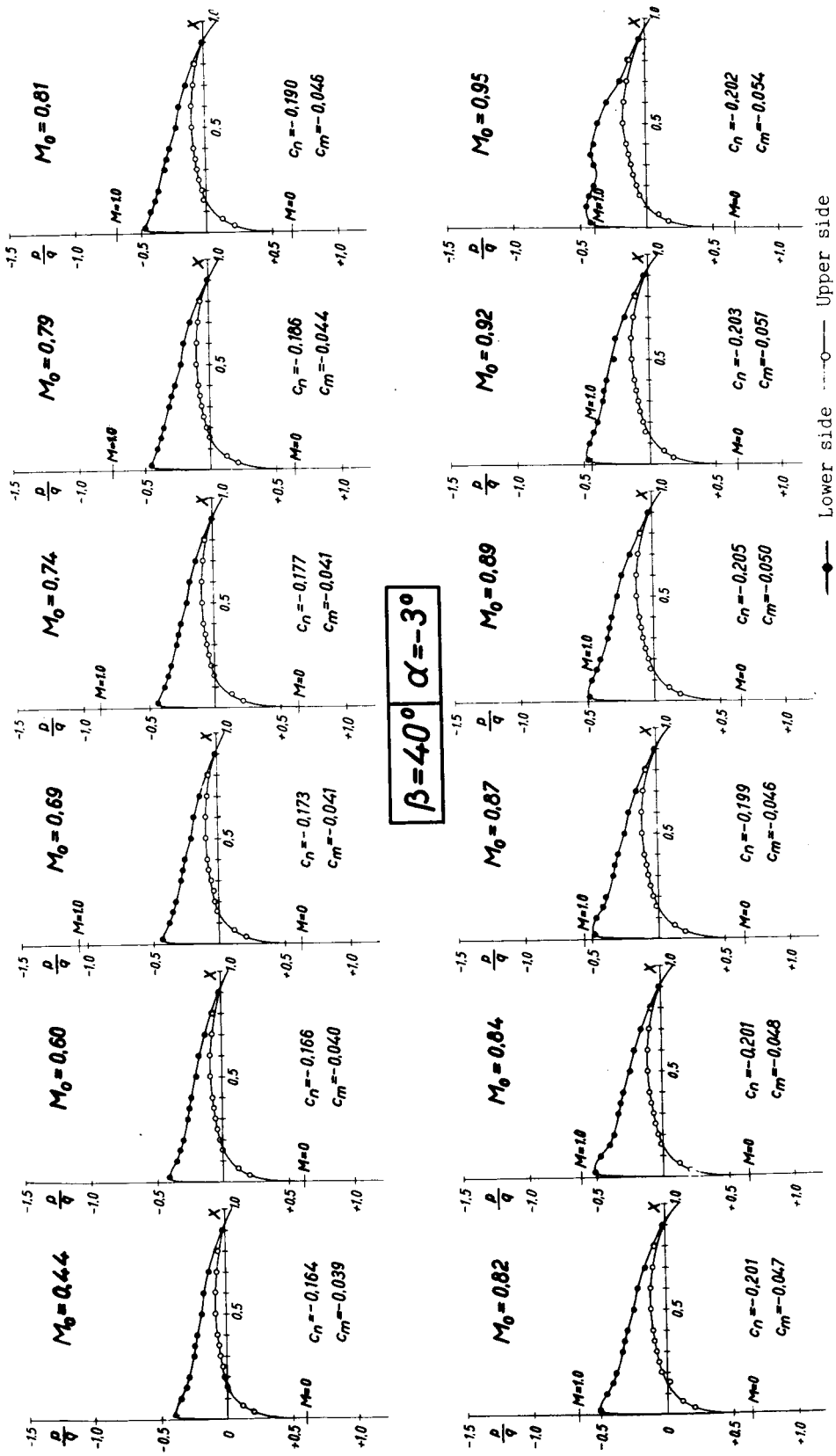
β=40° α=-3°
M₀=0.81
M₀=0.79
M₀=0.74
M₀=0.69
M₀=0.60
M₀=0.44
M₀=0.95
M₀=0.92
M₀=0.89
M₀=0.87
M₀=0.84
M₀=0.82
Lower side
Upper side

Figure 24.

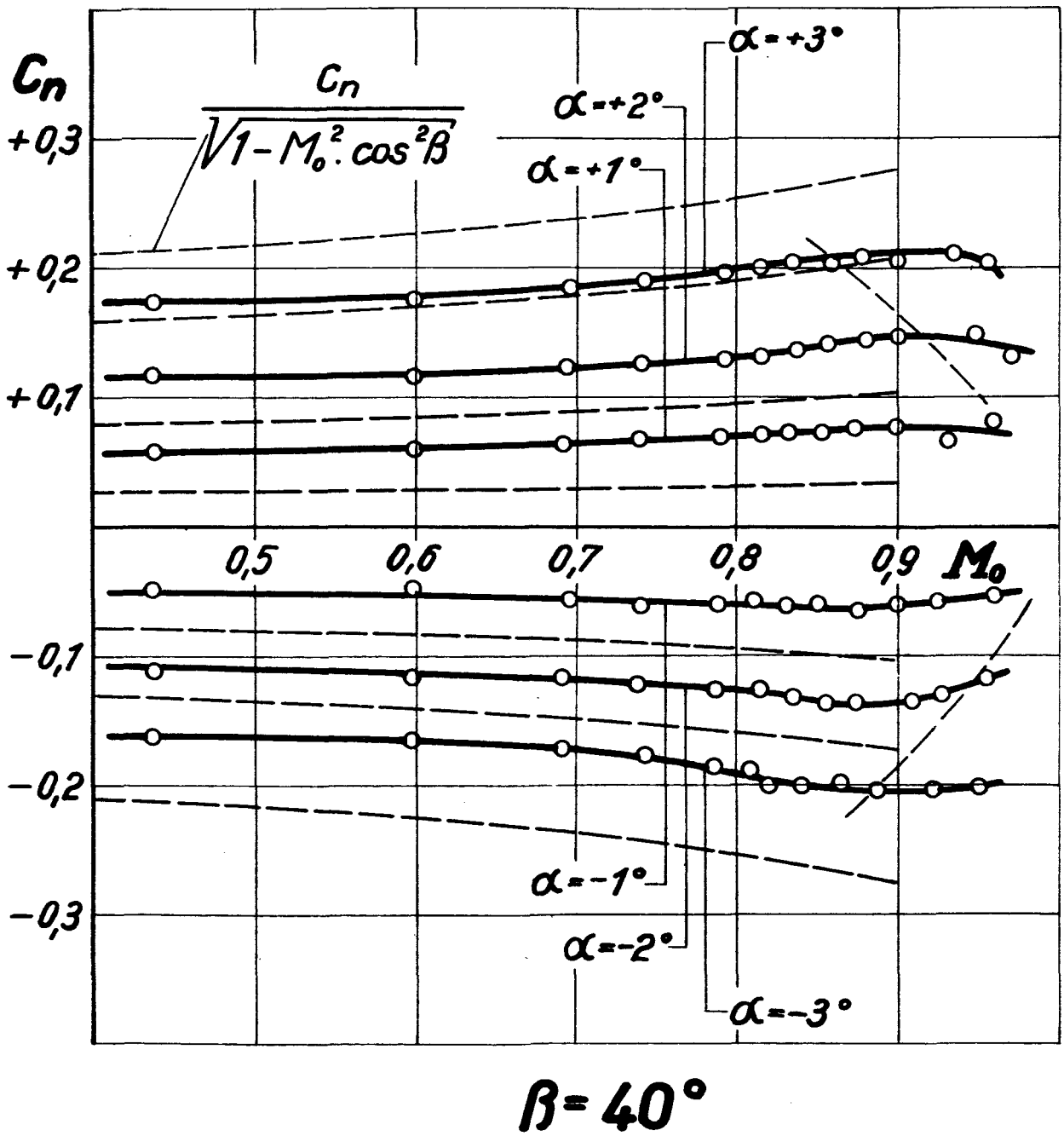
C_n
$\frac{C_n}{\sqrt{1-M_0^2 \cdot \cos^2\beta}}$
+0,3
+0,2
+0,1
−0,1
−0,2
−0,3
0,5
0,6
0,7
0,8
0,9
M_0
α=+3°
α=+2°
α=+1°
α=−1°
α=−2°
α=−3°
β=40°

Figure 25.

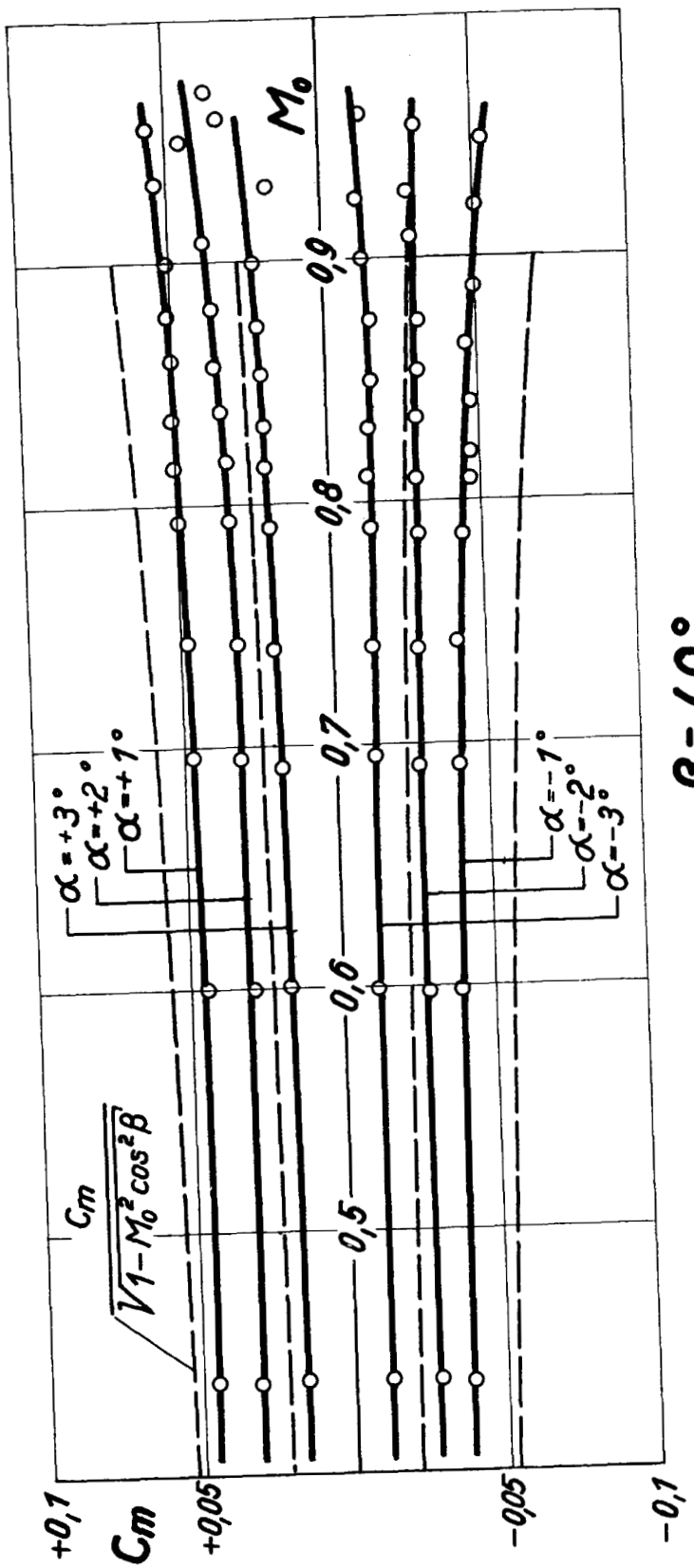
+0,1
Cm
+0,05
Cm / √(1−M₀² cos²β)
M₀
0,5
0,6
0,7
0,8
0,9
α=+3°
α=+2°
α=+1°
α=−1°
α=−2°
α=−3°
β=40°
−0,05
−0,1

Figure 26.

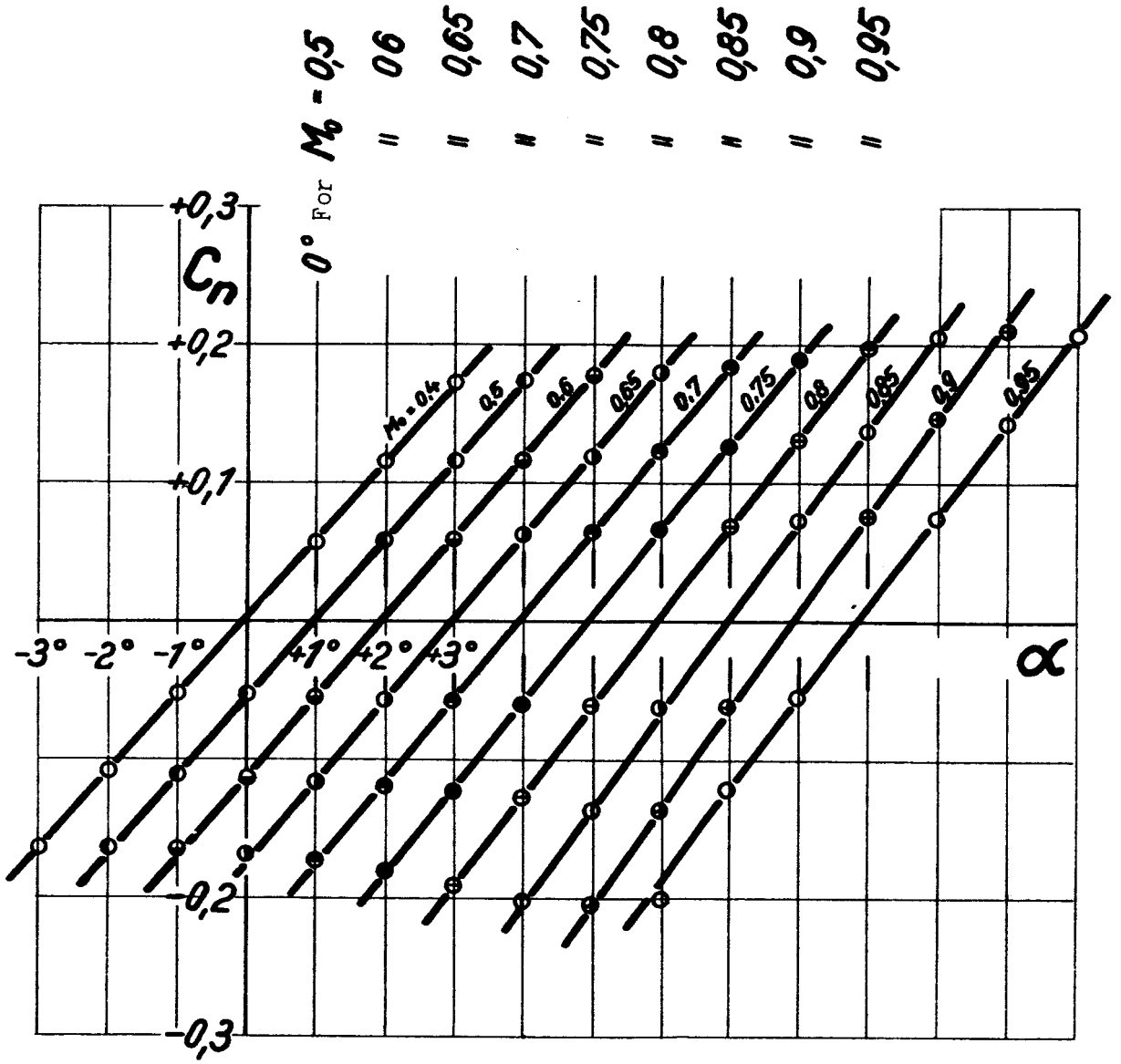

$\beta = 40°$

Figure 27.

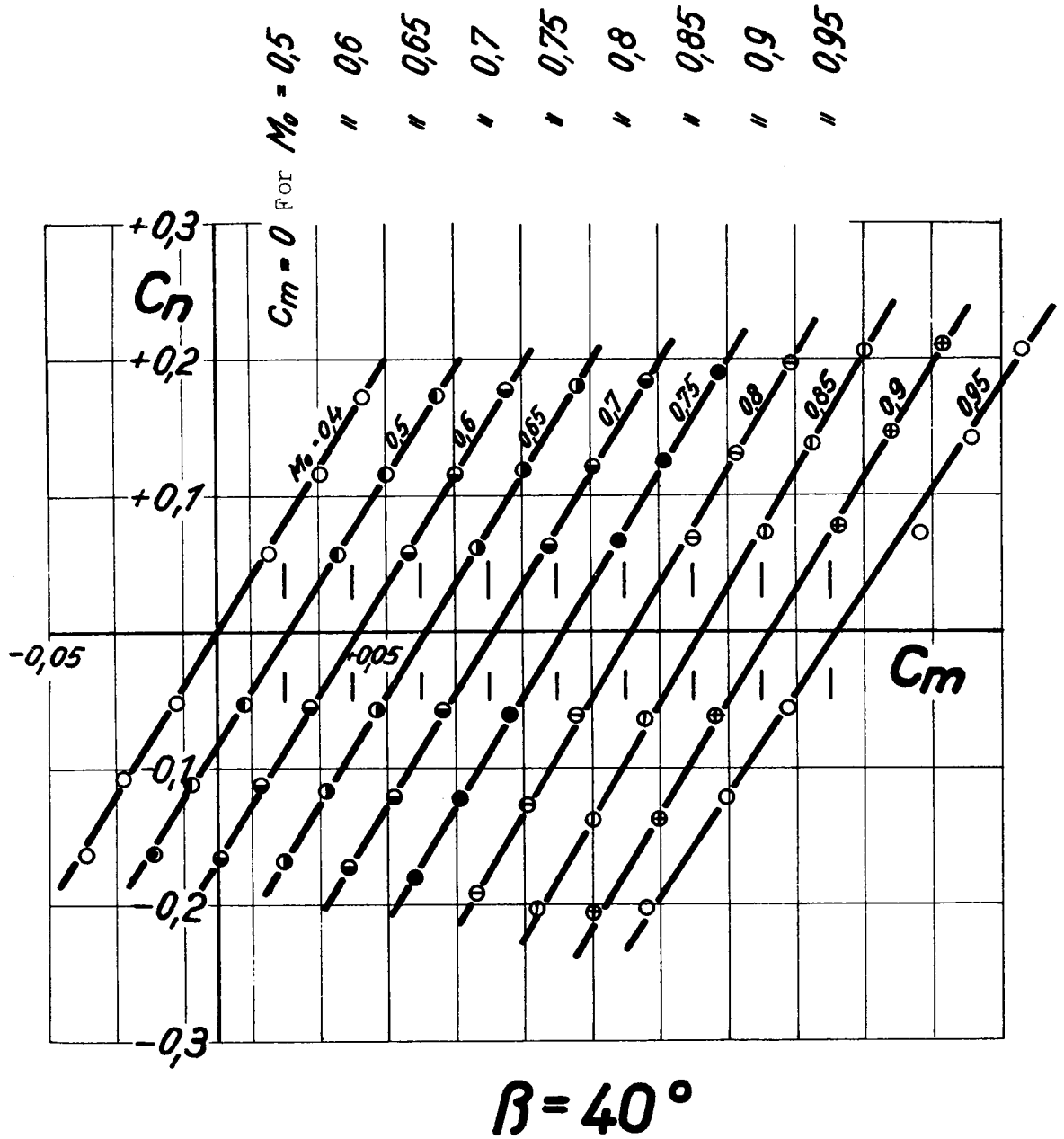
For Cm = 0
M₀ = 0,5
" 0,6
" 0,65
" 0,7
" 0,75
" 0,8
" 0,85
" 0,9
" 0,95
+0,3
Cn
+0,2
+0,1
-0,05
-0,1
-0,2
-0,3
M₀ .04
0,5
0,6
0,65
0,7
0,75
0,8
0,85
0,9
0,95
+0,05
Cm
β = 40°

Figure 28.

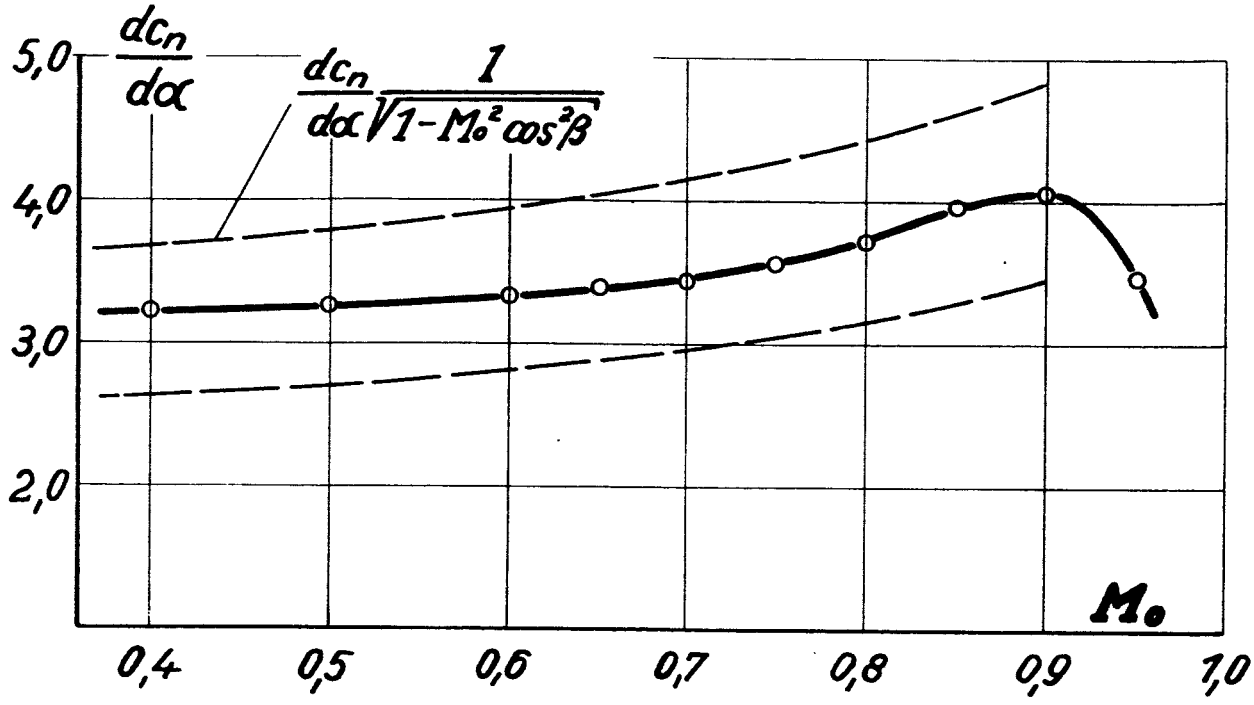
$\frac{dc_n}{d\alpha}$
$\frac{dc_n}{d\alpha}\frac{1}{\sqrt{1-M_o^2\cos^2\beta}}$
5,0
4,0
3,0
2,0
0,4
0,5
0,6
0,7
0,8
0,9
1,0
M_o

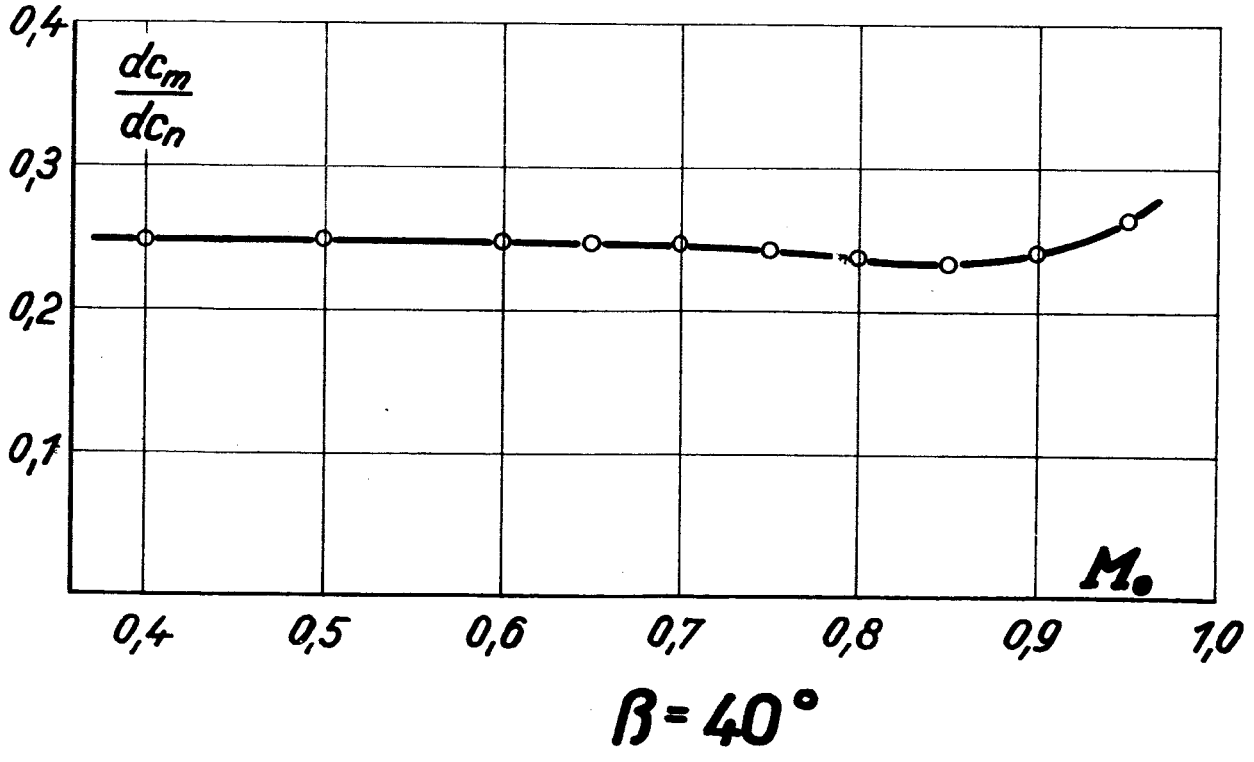
$\frac{dc_m}{dc_n}$
0,4
0,3
0,2
0,1
0,4
0,5
0,6
0,7
0,8
0,9
1,0
M_o
$\beta = 40°$

Figure 29.

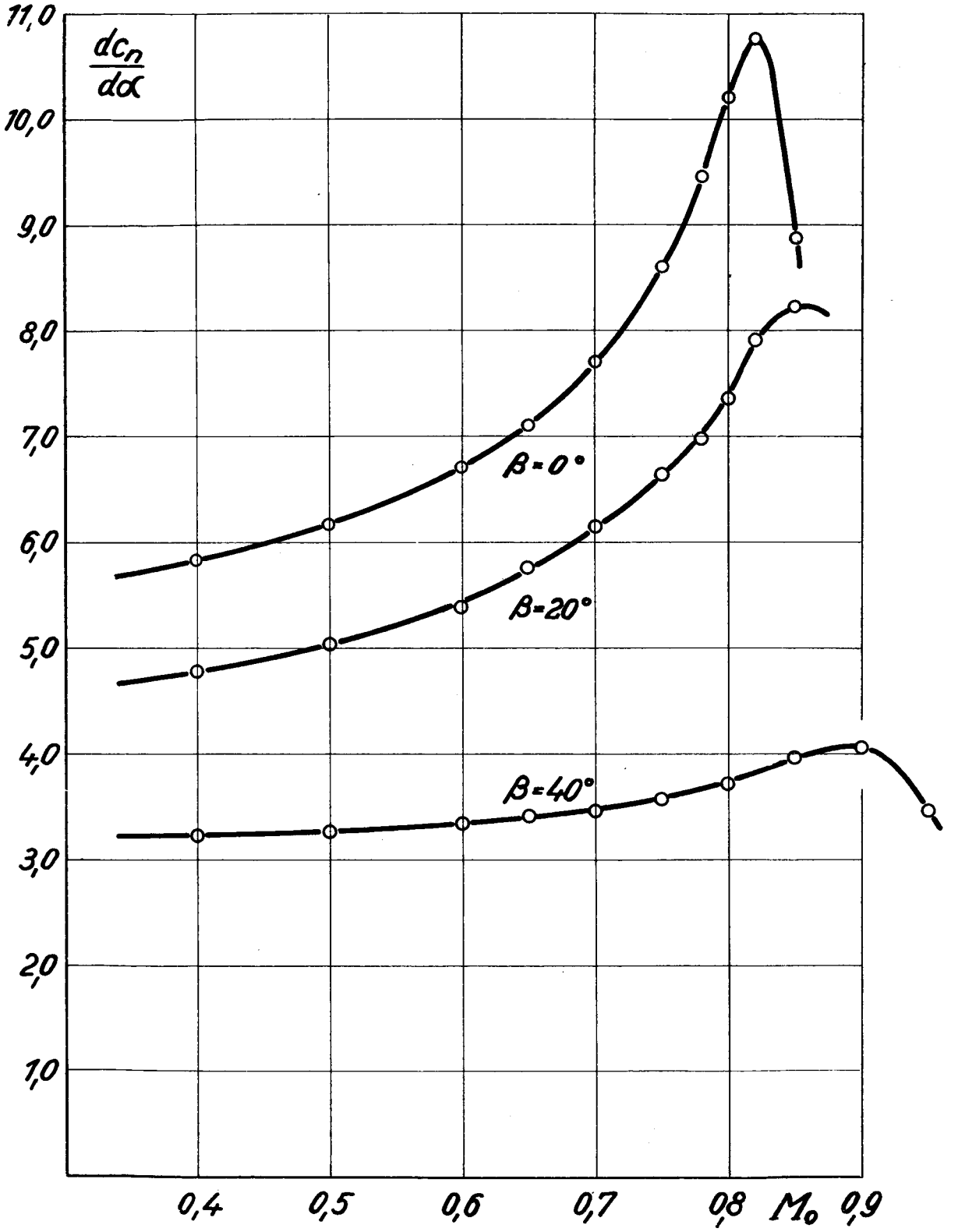
11,0
10,0
9,0
8,0
7,0
6,0
5,0
4,0
3,0
2,0
1,0
$\frac{dc_n}{d\alpha}$
β=0°
β=20°
β=40°
0,4
0,5
0,6
0,7
0,8
M_o
0,9

Figure 30.

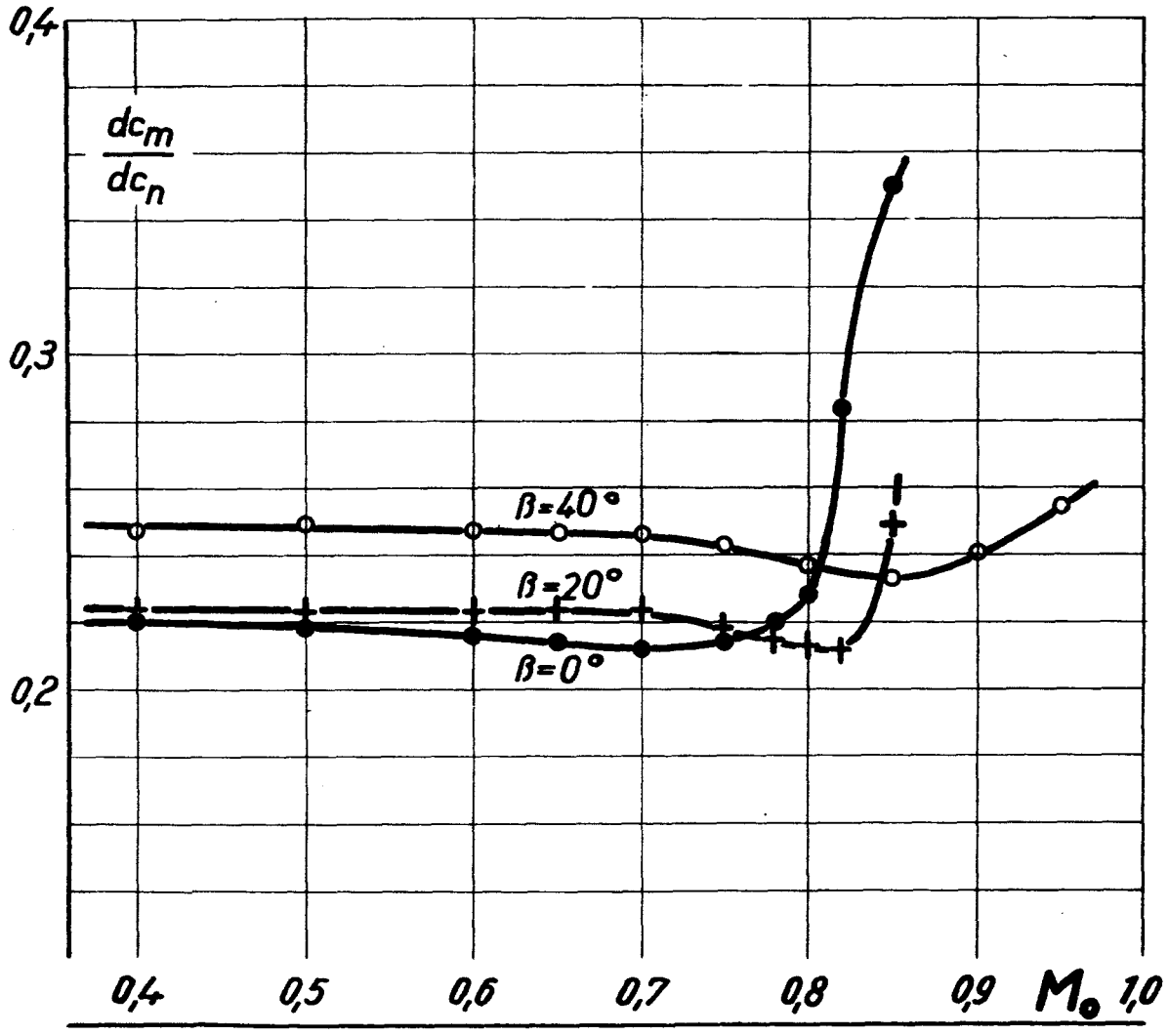

Figure 31.

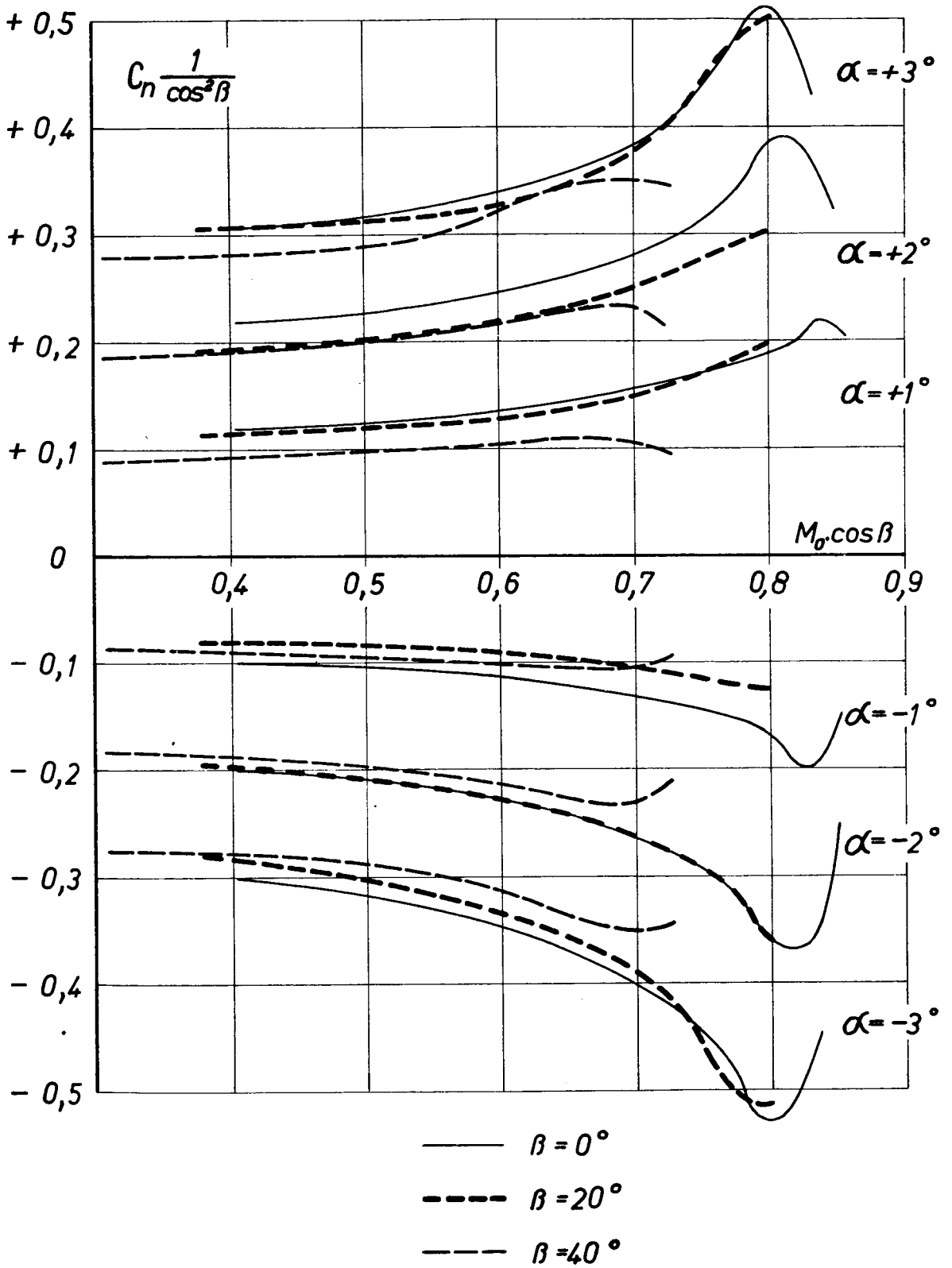
+ 0,5
+ 0,4
+ 0,3
+ 0,2
+ 0,1
0
- 0,1
- 0,2
- 0,3
- 0,4
- 0,5
$C_n \frac{1}{\cos^2 \beta}$
$M_0 \cdot \cos \beta$
0,4
0,5
0,6
0,7
0,8
0,9
$\alpha = +3°$
$\alpha = +2°$
$\alpha = +1°$
$\alpha = -1°$
$\alpha = -2°$
$\alpha = -3°$
$\beta = 0°$
$\beta = 20°$
$\beta = 40°$

Figure 32.

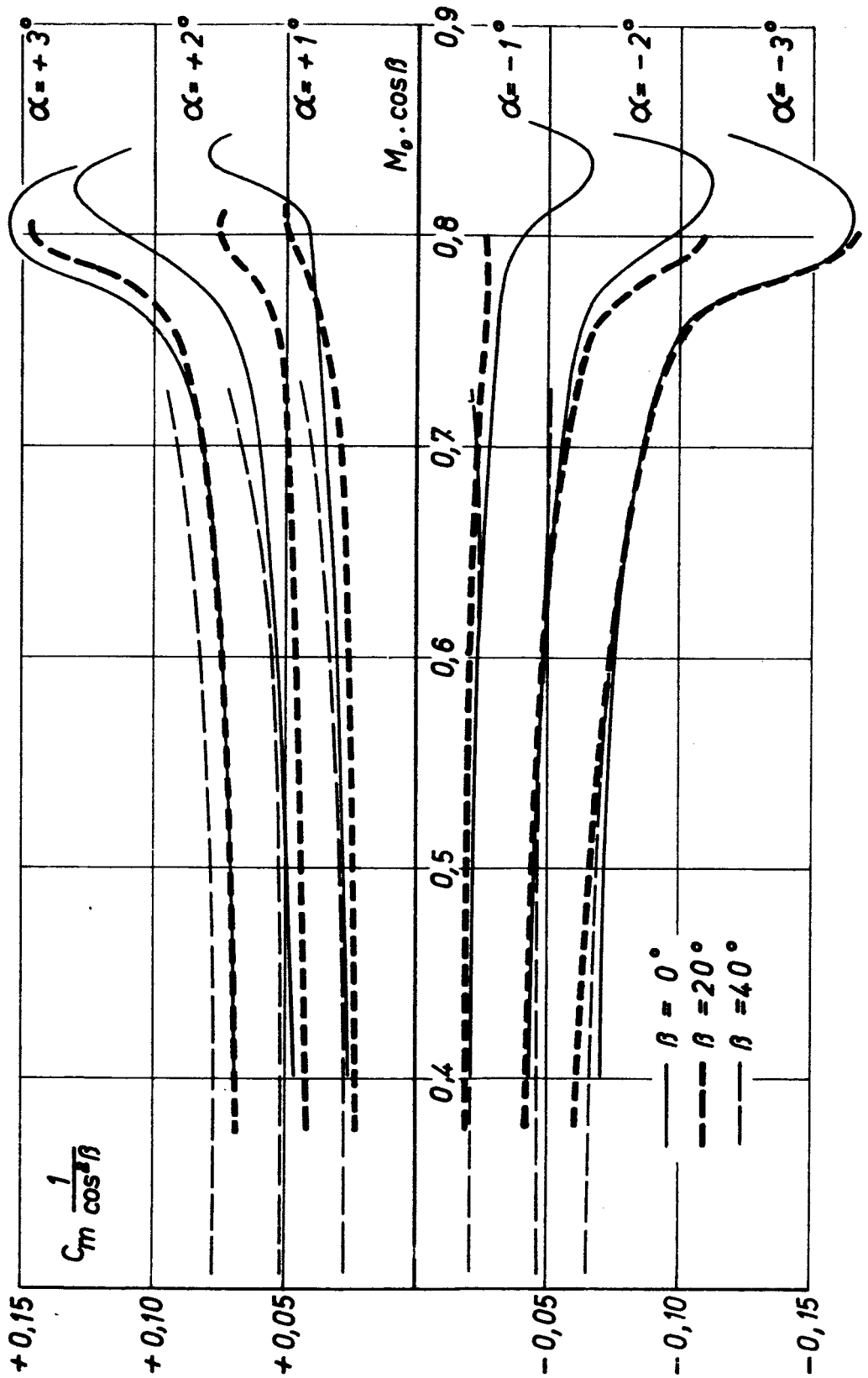
α = +3°
α = +2°
α = +1°
α = -1°
α = -2°
α = -3°
$M_0 \cdot \cos\beta$
0,4
0,5
0,6
0,7
0,8
0,9
$c_m \frac{1}{\cos^2\beta}$
+0,15
+0,10
+0,05
-0,05
-0,10
-0,15
β = 0°
β = 20°
β = 40°

Figure 33.

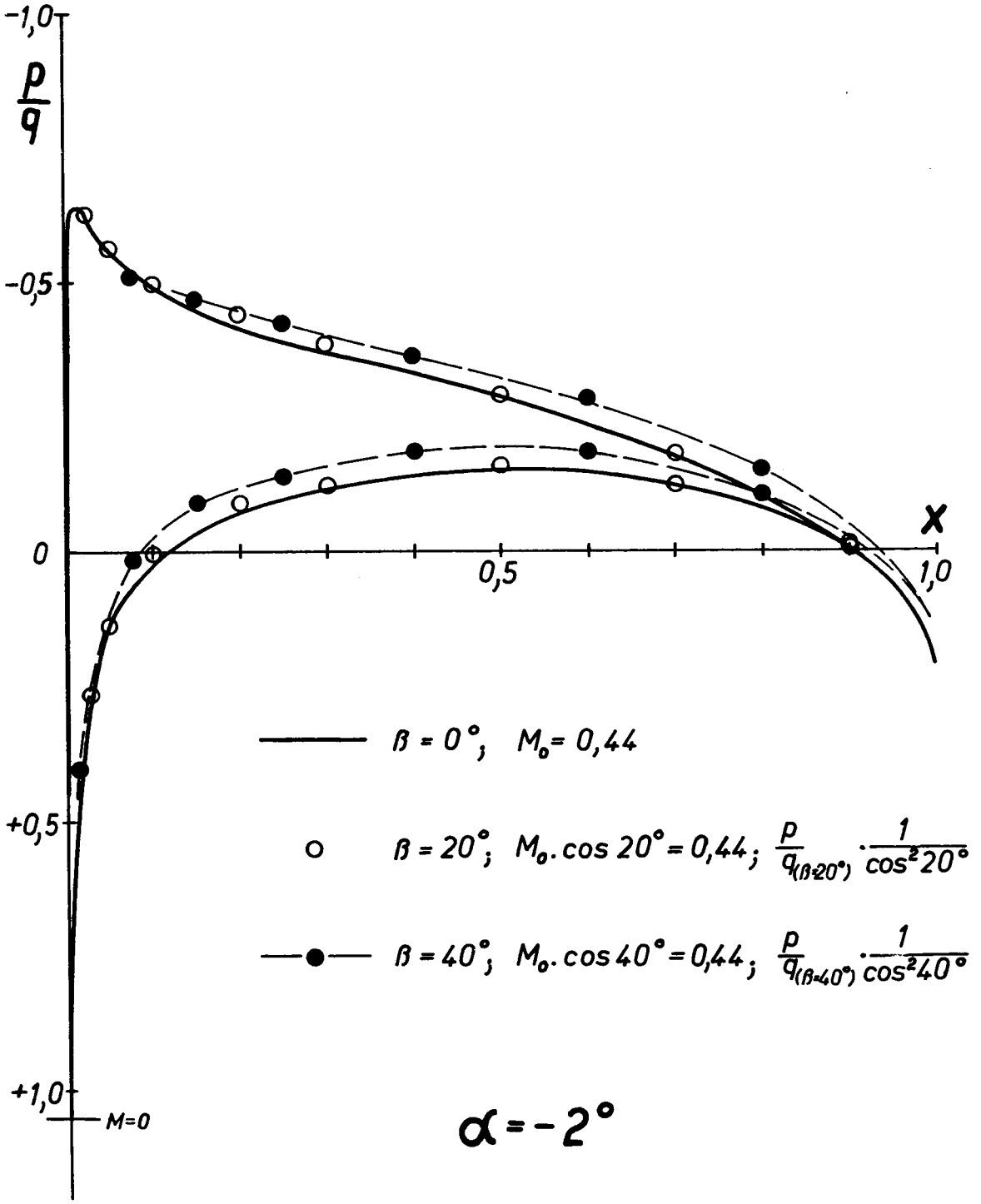
-1,0
p/q
-0,5
0
0,5
1,0
X
+0,5
+1,0
M=0
β = 0°; M₀ = 0,44
β = 20°; M₀. cos 20° = 0,44; p/q(β=20°) · 1/cos²20°
β = 40°; M₀. cos 40° = 0,44; p/q(β=40°) · 1/cos²40°
α = -2°

Figure 34.

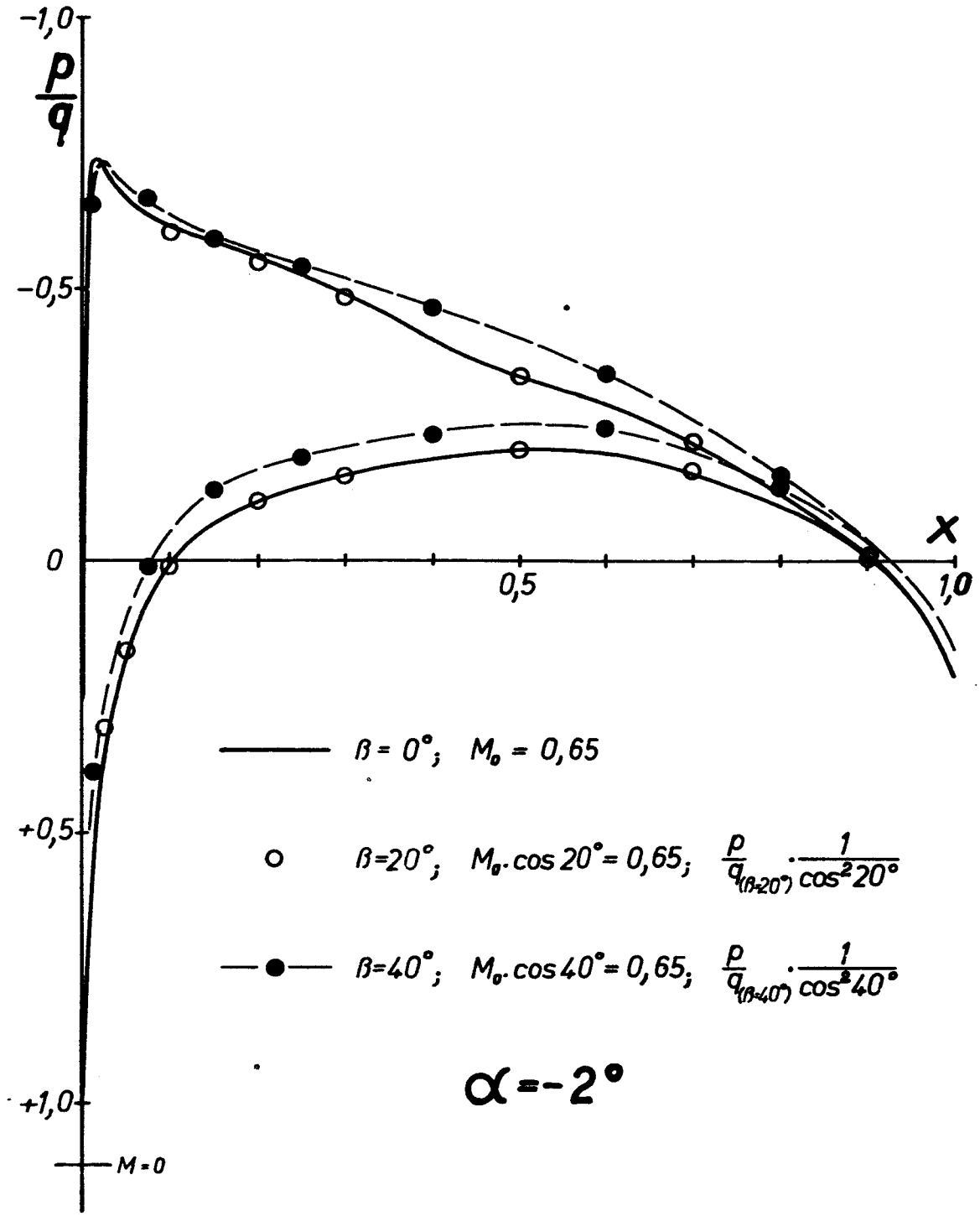
-1,0
p/q
-0,5
0
0,5
1,0
x
+0,5
+1,0
M=0
β = 0°; M₀ = 0,65
β=20°; M₀·cos 20° = 0,65; p/q(β=20°) · 1/cos²20°
β=40°; M₀·cos 40° = 0,65; p/q(β=40°) · 1/cos²40°
α=-2°

Figure 35.

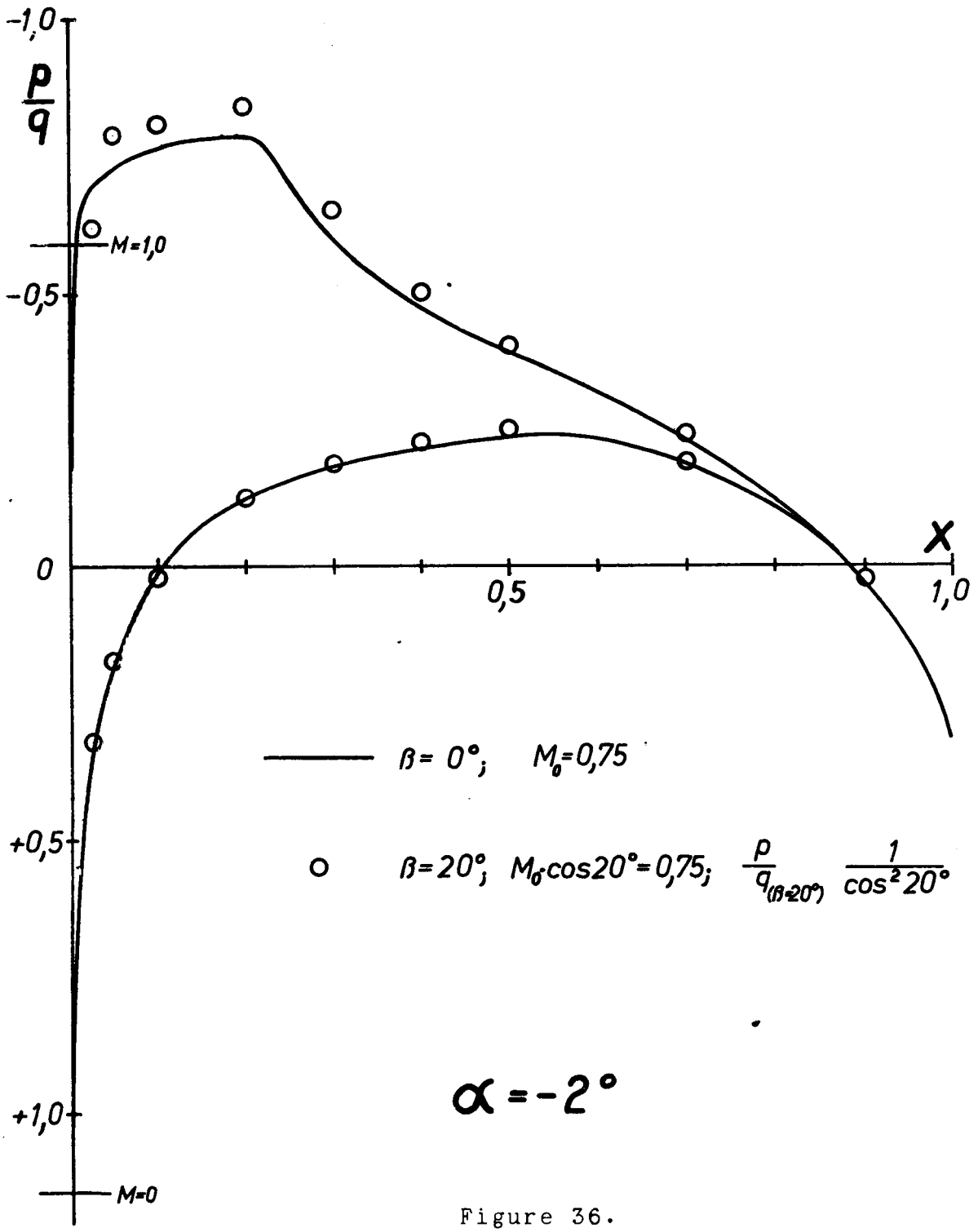
-1,0
p/q
M=1,0
-0,5
0
0,5
1,0
X
+0,5
+1,0
M=0
β= 0°; M₀=0,75
β=20°; M₀cos20°=0,75; p/q(β=20°) 1/cos²20°
α=-2°

Figure 36.

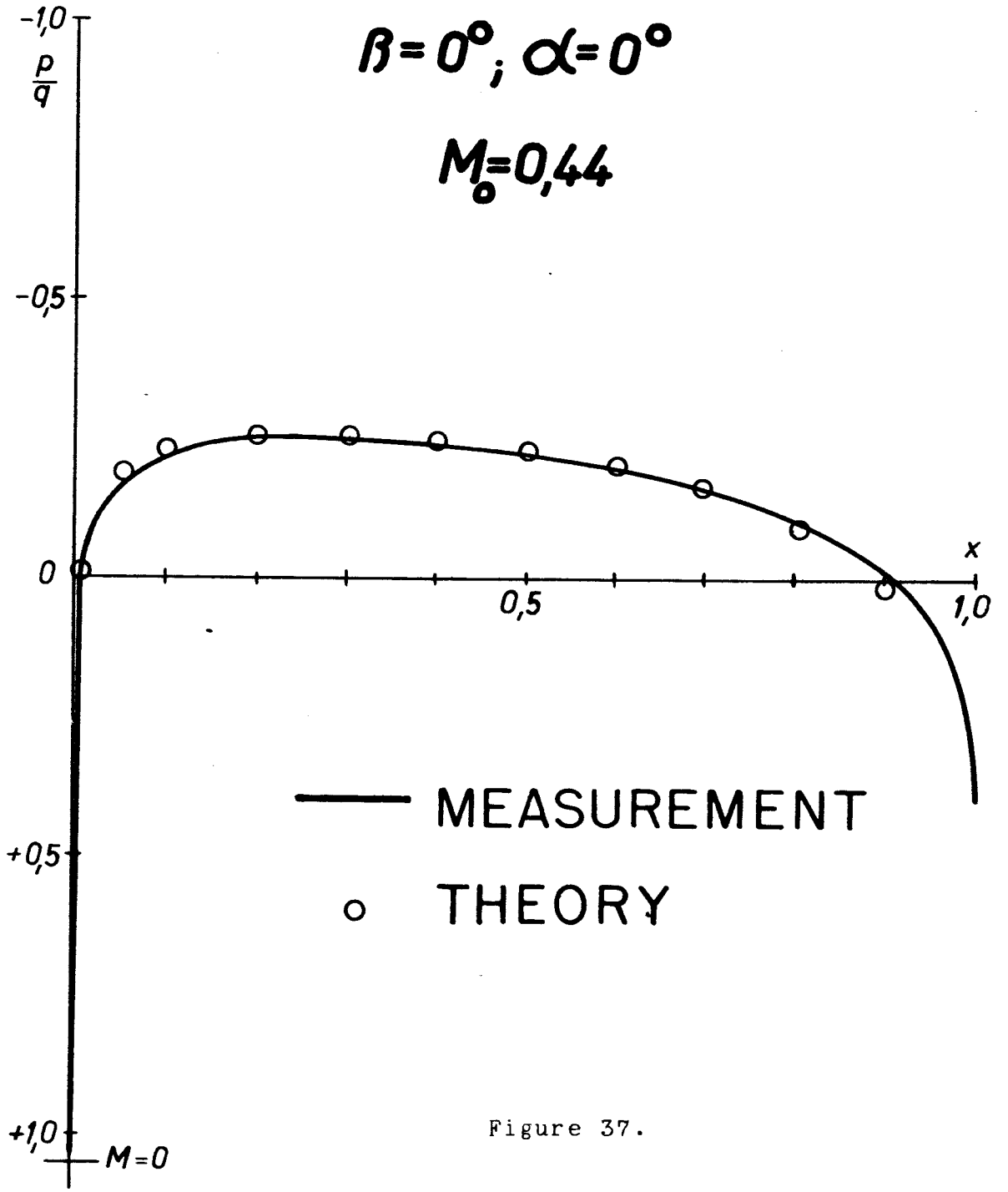

Figure 37.

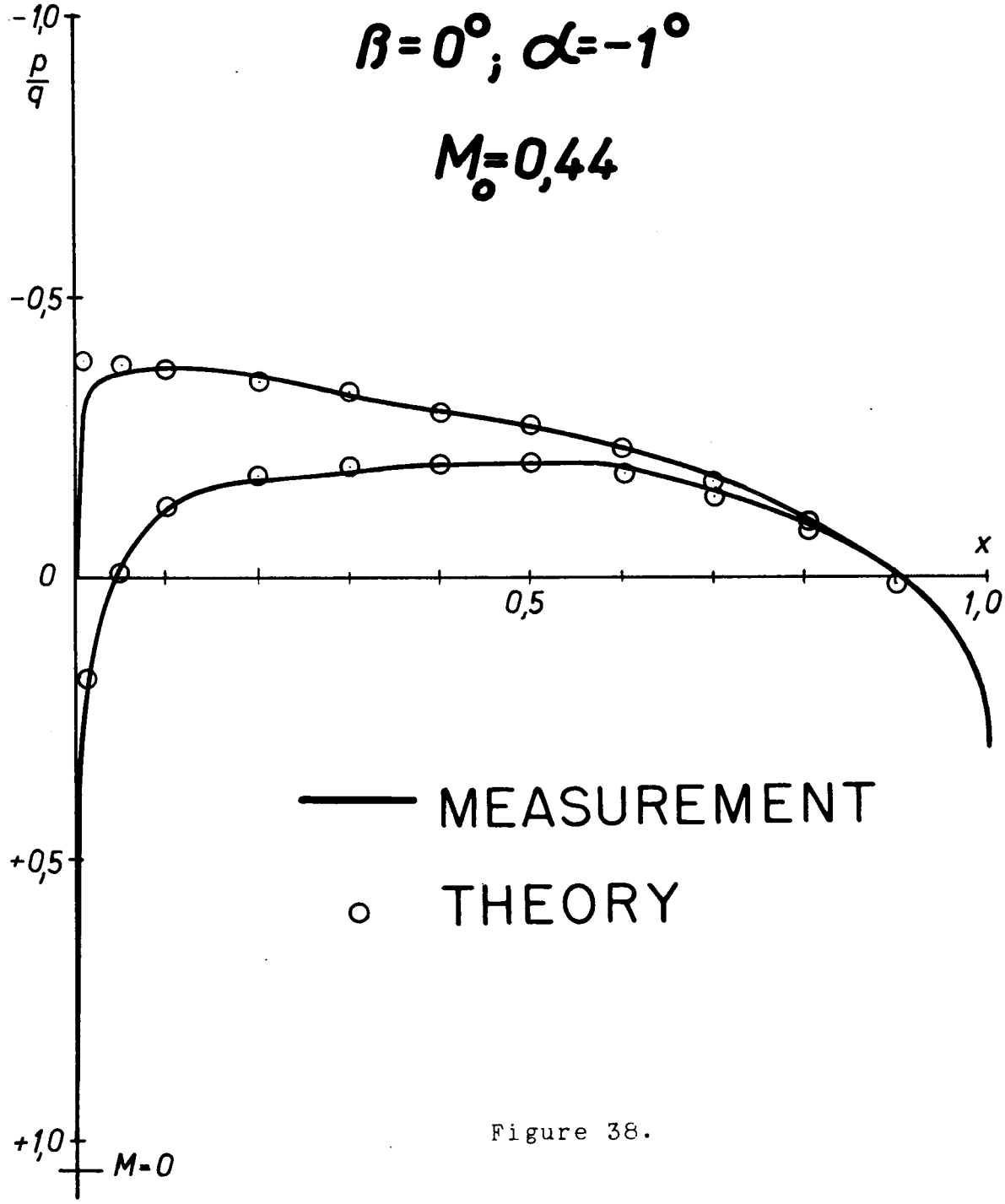

Figure 38.

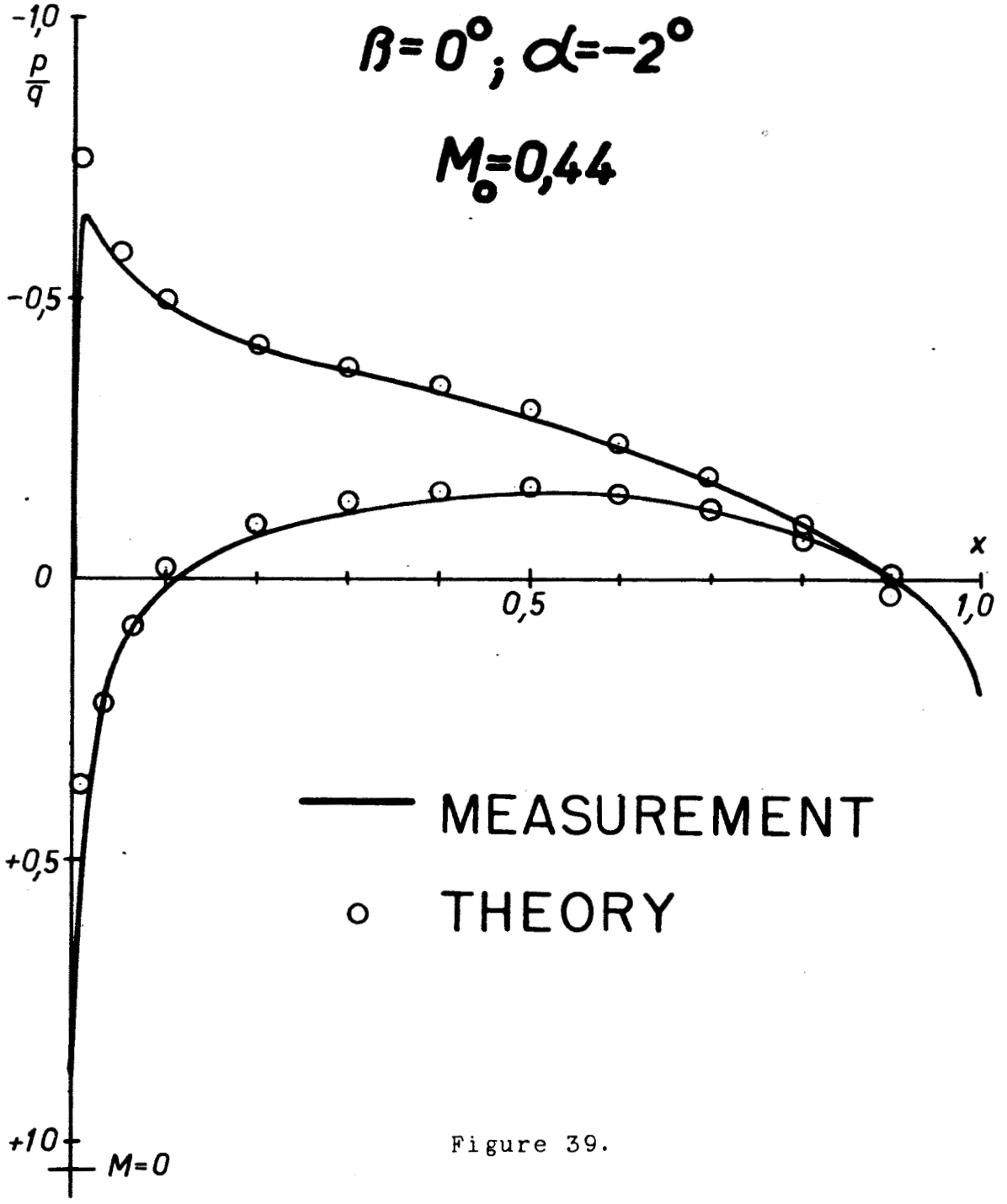

Figure 39.

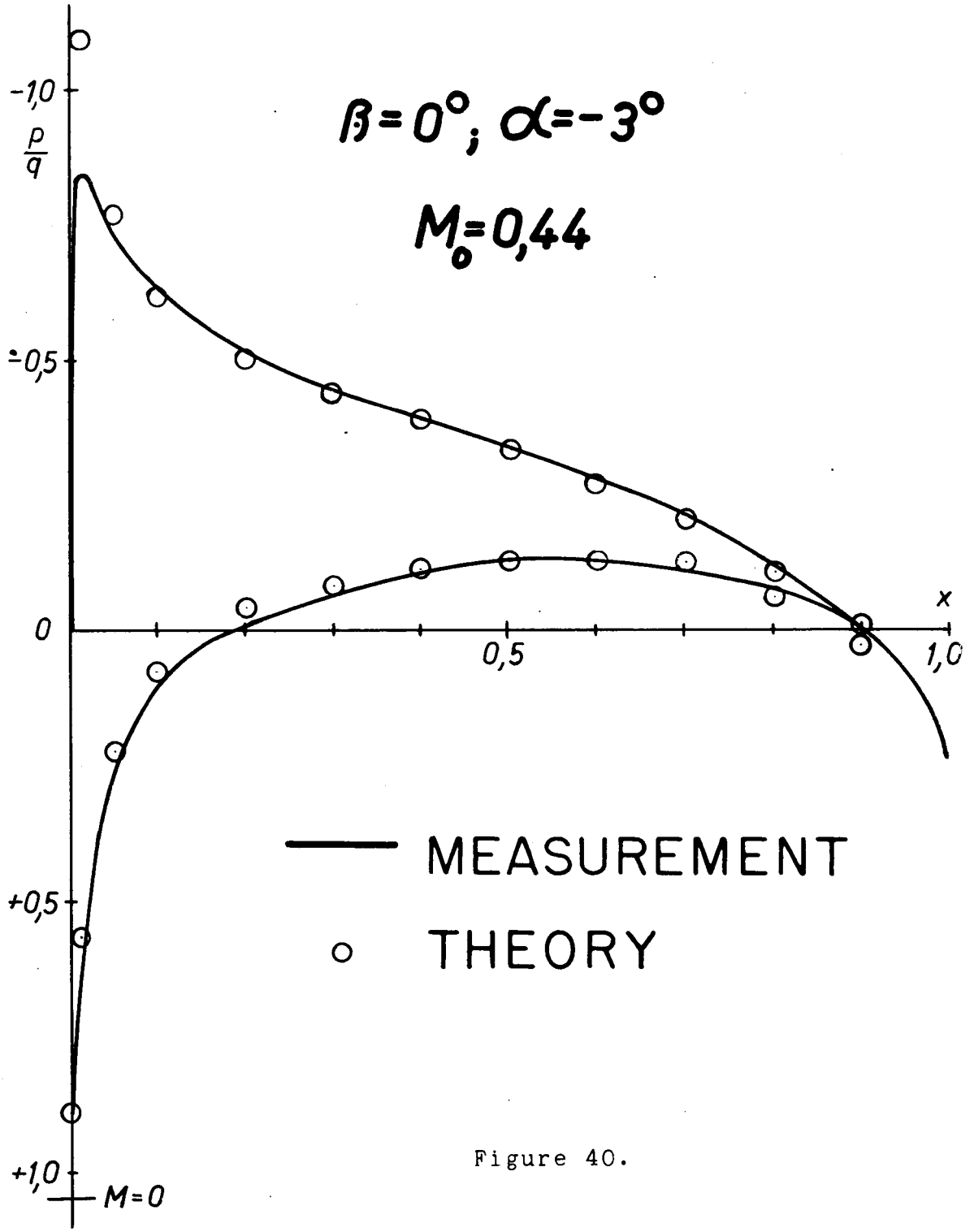

Figure 40.

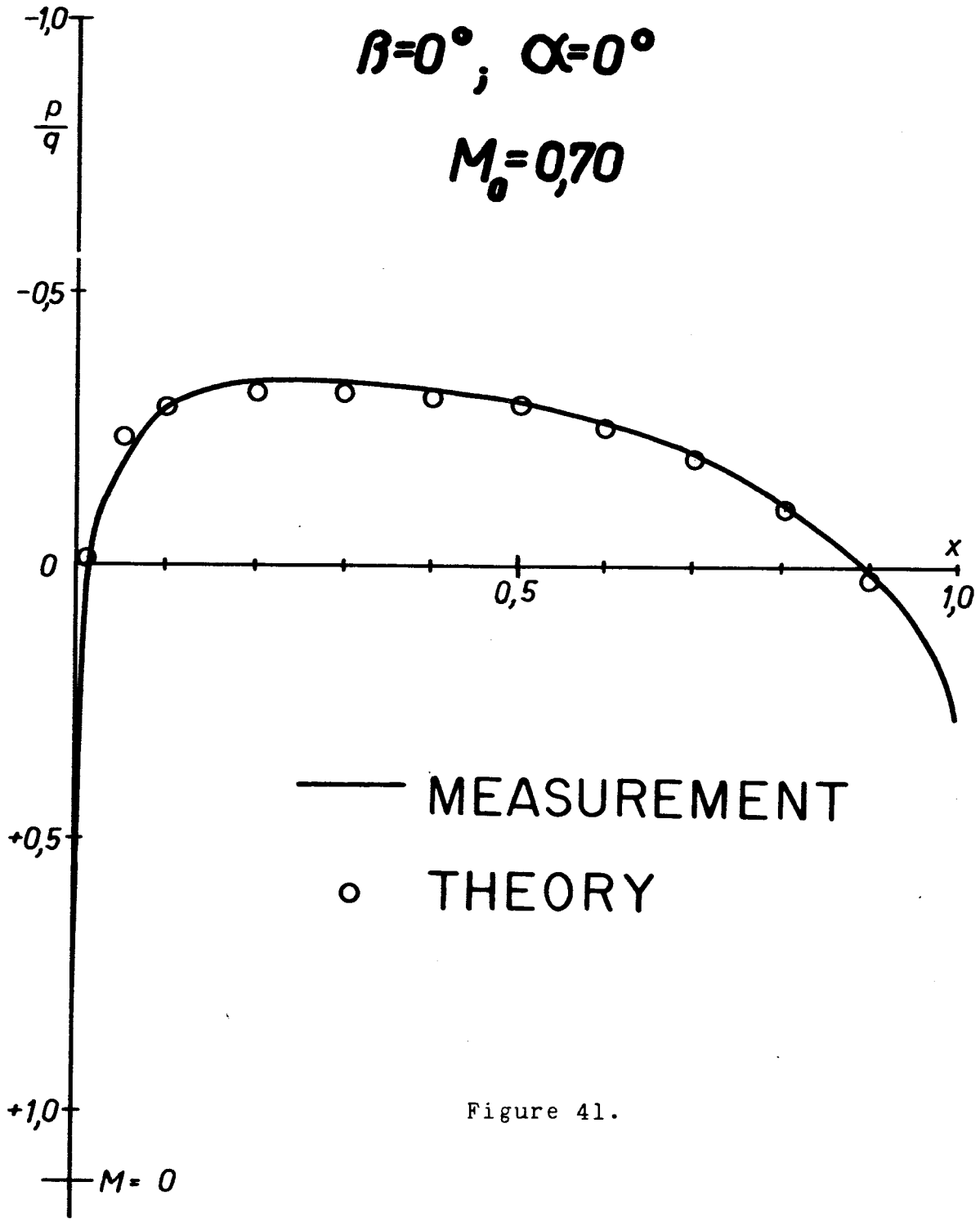

Figure 41.

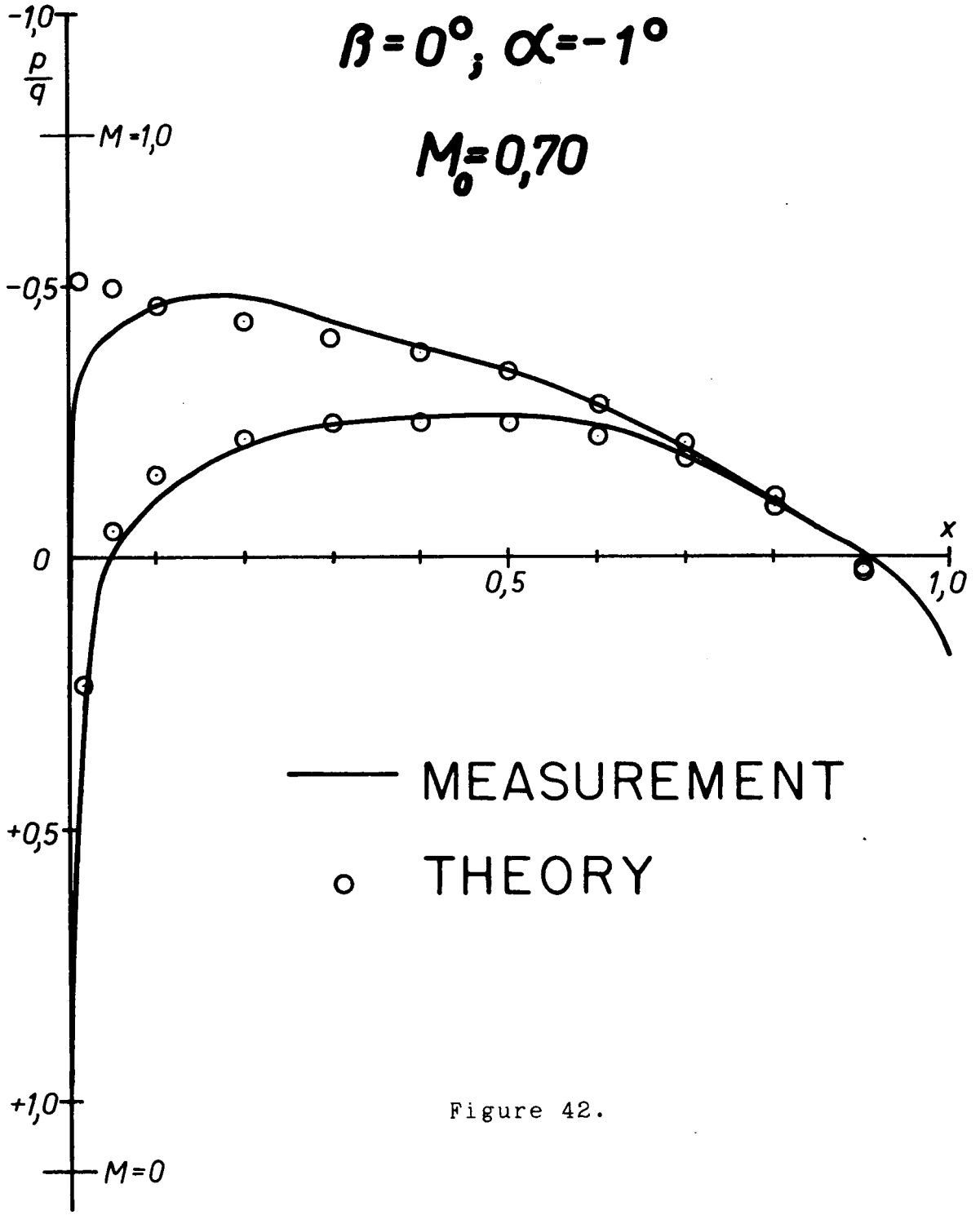

Figure 42.

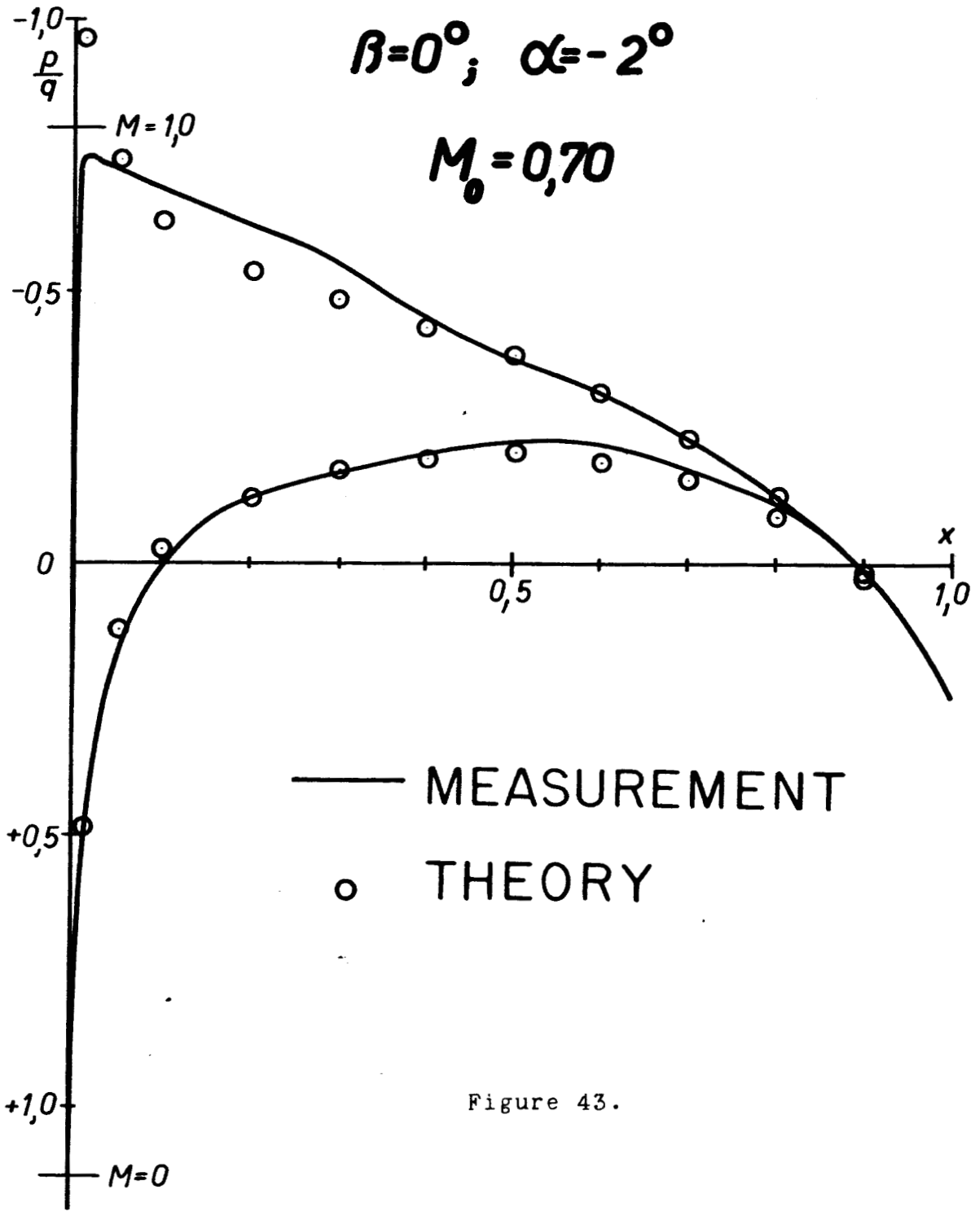

Figure 43.

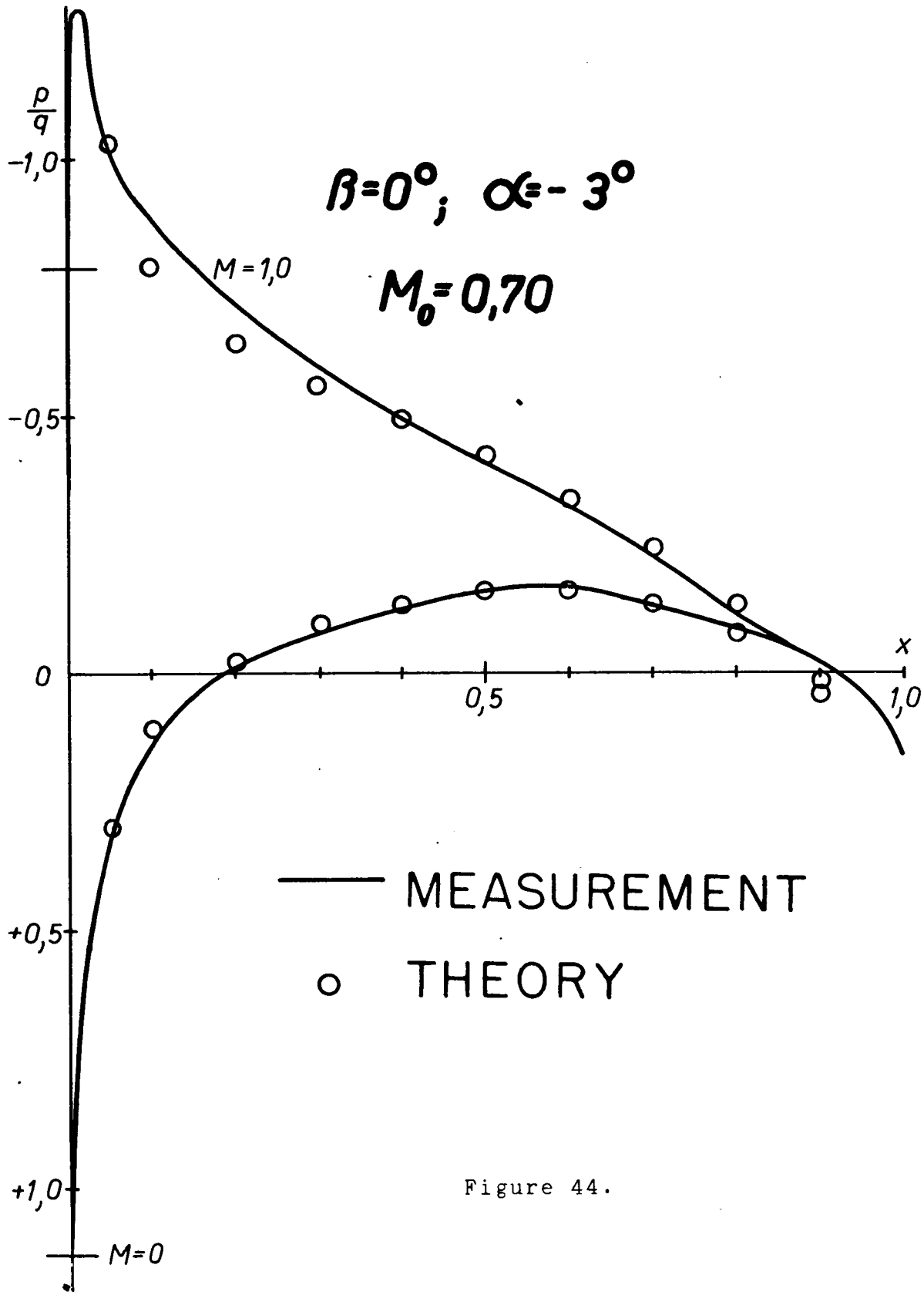

Figure 44.

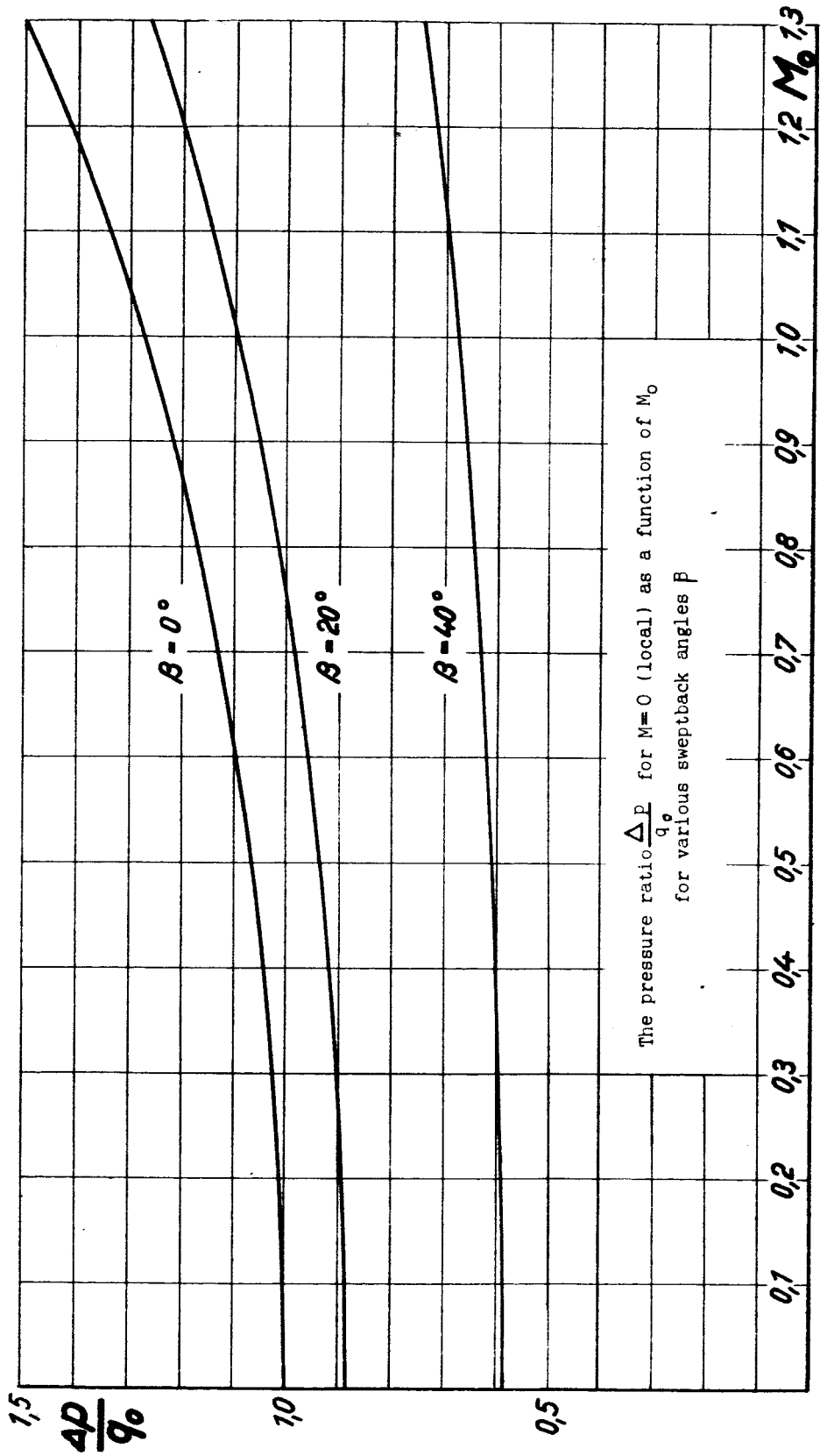
1,5
1,0
0,5
$\frac{\Delta p}{q_o}$
0,1
0,2
0,3
0,4
0,5
0,6
0,7
0,8
0,9
1,0
1,1
1,2
1,3
M_o
β = 0°
β = 20°
β = 40°
The pressure ratio $\frac{\Delta p}{q_o}$ for M=0 (local) as a function of M_o
for various sweptback angles β

Figure 45.

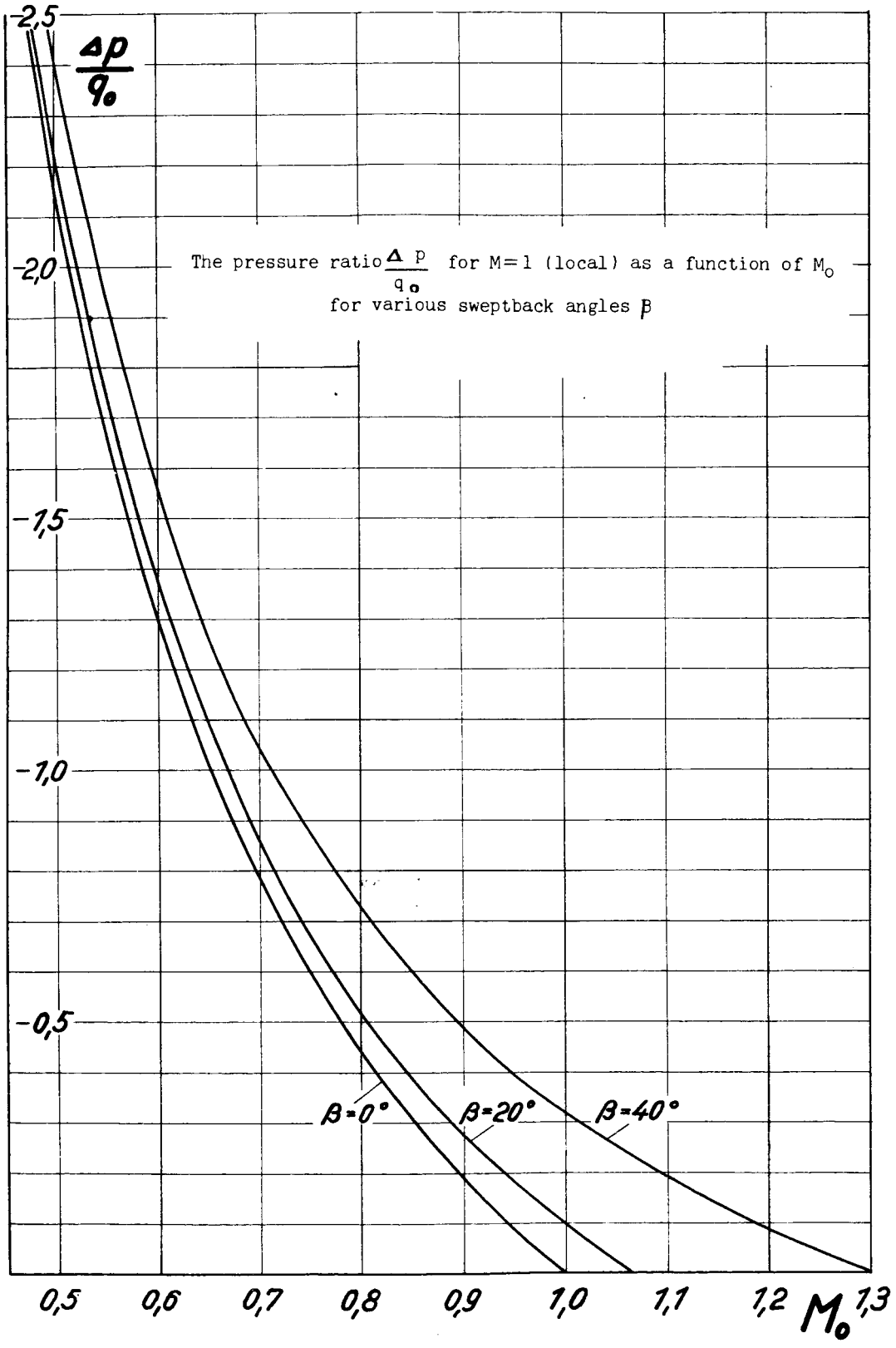
-2,5
Δp/q₀
-2,0
The pressure ratio Δ p / q₀ for M=1 (local) as a function of M₀
for various sweptback angles β
-1,5
-1,0
-0,5
β=0°
β=20°
β=40°
0,5
0,6
0,7
0,8
0,9
1,0
1,1
1,2
M₀
1,3

Figure 46.